The Astrophysical Journal Letters, 971:L12 (21pp), 2024 August 10 https://doi.org/10.3847/2041-8213/ad5b52

TOI-1685 b Is a Hot Rocky Super-Earth: Updates to the Stellar and Planet Parameters of a Popular JWST Cycle 2 Target

Jennifer A. Burt[1], Matthew J. Hooton[2], Eric E. Mamajek[1], Oscar Barragán[3], Sarah C. Millholland[4], Tyler R. Fairnington[5], Chloe Fisher[3], Samuel P. Halverson[1], Chelsea X. Huang[5], Madison Brady[6], Andreas Seifahrt[6], Eric Gaidos[7,8], Rafael Luque[6], David Kasper[6], and Jacob L. Bean[6]
[1] Jet Propulsion Laboratory, California Institute of Technology, 4800 Oak Grove Drive, Pasadena, CA 91109, USA
[2] Cavendish Laboratory, JJ Thomson Avenue, Cambridge CB3 0HE, UK
[3] Astrophysics, University of Oxford, Denys Wilkinson Building, Keble Road, Oxford, OX1 3RH, UK
[4] Department of Physics, Massachusetts Institute of Technology, Cambridge, MA 02139, USA; MIT Kavli Institute for Astrophysics and Space Research, Massachusetts Institute of Technology, Cambridge, MA 02139, USA
[5] Centre for Astrophysics, University of Southern Queensland, West Street, Toowoomba, QLD 4350, Australia
[6] Department of Astronomy & Astrophysics, University of Chicago, Chicago, IL, USA
[7] Department of Earth Sciences, University of Hawai'i at Mānoa, 1680 East-West Road, Honolulu, HI 96822, USA
[8] Institute for Astrophysics, University of Vienna, Türkenschanzstrasse 17, A-1180 Vienna, Austria
Received 2024 February 15; revised 2024 May 3; accepted 2024 May 11; published 2024 August 9

Abstract

We present an updated characterization of the TOI-1685 planetary system, which consists of a $P_b = 0.69$ day ultra-short-period super-Earth planet orbiting a nearby ($d = 37.6$ pc) M2.5V star (TIC 28900646, 2MASS J04342248 +4302148). This planet was previously featured in two contemporaneous discovery papers, but the best-fit planet mass, radius, and bulk density values were discrepant, allowing it to be interpreted either as a hot, bare rock or a 50% H_2O/50% $MgSiO_3$ water world. TOI-1685 b will be observed in three independent JWST Cycle 2 programs, two of which assume the planet is a water world, while the third assumes that it is a hot rocky planet. Here we include a refined stellar classification with a focus on addressing the host star's metallicity, an updated planet radius measurement that includes two sectors of TESS data and multicolor photometry from a variety of ground-based facilities, and a more accurate dynamical mass measurement from a combined CARMENES, InfraRed Doppler, and MAROON-X radial velocity data set. We find that the star is very metal-rich ([Fe/H] $\simeq +0.3$) and that the planet is systematically smaller, lower mass, and higher density than initially reported, with new best-fit parameters of $R_{pl} = 1.468\ ^{+0.050}_{-0.051}\ R_\oplus$ and $M_{pl} = 3.03^{+0.33}_{-0.32}\ M_\oplus$. These results fall in between the previously derived values and suggest that TOI-1685 b is a hot rocky planet with an Earth-like density ($\rho_{pl} = 5.3 \pm 0.8$ g cm^{-3}, or 0.96 $\rho_\oplus$), high equilibrium temperature ($T_{eq} = 1062 \pm 27$ K), and negligible volatiles, rather than a water world.

Unified Astronomy Thesaurus concepts: Exoplanets (498); Super Earths (1655); Radial velocity (1332); Transit photometry (1709)

Materials only available in the online version of record: machine-readable tables

1. Introduction

To date, NASA's TESS mission (Ricker et al. 2015; Guerrero et al. 2021) has surveyed 93% of the sky for at least 28 days and has detected over 1900 super-Earth- and sub-Neptune-sized planet candidates.[9] Many of these candidates are enticing targets for atmospheric follow-up studies with missions such as the Hubble and James Webb Space Telescopes (HST and JWST, respectively) thanks to the relatively bright magnitudes of their host stars. Indeed, of the 52 unique planets selected for transit observations with JWST in Cycle 2, 32 were first detected by TESS.[10]

Assessment of a planet's potential for such observations and the eventual interpretation of its atmospheric spectrum is reliant upon accurate and precise measurements of the planet's radius and mass, which together dictate its scale height. As these properties are both obtained via indirect detection methods (generally transit photometry for the radius and radial velocity (RV) spectroscopy for the mass), accurate and precise knowledge of the host star's radius and mass is also crucial, as these factor into the derived planet parameters.

Here we present an updated analysis and refined stellar and planetary parameters for one such small planet, TOI-1685 b. The planet was first published in a set of independent discovery papers: Bluhm et al. (2021) and Hirano et al. (2021), hereafter denoted as B21 and H21, respectively. Both papers included photometry from TESS Sector 19 in their analyses, but the variety in the additional data sets incorporated and the analysis methods used between the two publications led to significant disagreements in their adopted values of stellar mass, stellar radius, and planetary radius. Although the constraints on the RV semiamplitude and planet mass derived from the CARMENES RV data used in B21 and the InfraRed Doppler (IRD) RV data used in H21 are consistent to within 1σ, the corresponding planetary densities differ significantly due to different measurements of the planet's radius. B21 find a best-fit planet radius of $R_{pl} = 1.70 \pm 0.07\ R_\oplus$, consistent with TOI-1685 b having a

[9] Based on the ExoFOP TOI Catalog as of 2024 January: https://exofop.ipac.caltech.edu/tess/view_toi.php.
[10] https://www.stsci.edu/jwst/science-execution/approved-programs/general-observers/cycle-2-go

significant (50%) water fraction, while H21 find a best-fit planet radius of $R_{pl} = 1.459 \pm 0.065\ R_{\oplus}$, which suggests the planet is a rocky super-Earth devoid of any significant water or volatile components. Luque & Pallé (2022) presented a joint analysis of the transit and RV data from both papers, adopting the stellar parameters from B21. Their derived system properties were in strong agreement with B21 but with a smaller best-fit mass, which further favored a significant water contribution to this planet's composition.

The proximity of the system, the planet's high planetary equilibrium temperature ($T_{\rm eq} \sim 1000$ K; B21 and H21), and the possibility of detecting atmospheric features in transmission and emission led to its inclusion in three successful JWST programs (Benneke et al. 2023; Fisher et al. 2023; Luque et al. 2023), all of which are scheduled for 2024. Two of these proposals hold TOI-1685 b up as a bona fide water world, while the third assumes the planet is a rocky super-Earth and aims to study oxidation in its potential atmosphere.

We revisit the characterization of TOI-1685 and its planet, incorporating new precise RV measurements taken with the MAROON-X spectrograph, additional ground-based photometry from the MuSCAT network, and an additional sector of TESS photometry. We include a study of the star's photometric metallicity, finding it to be metal-rich, which results in a smaller stellar radius value than the previously published estimates. We highlight the expanded transit photometry and RV data sets, along with the broadband photometry used in our analysis, in Section 2 and then detail the updated stellar, transit, and RV analyses in Section 3. We combine these results and present a refined interpretation of this system in Section 4, touching on the planet's likely characteristics and its potential for atmospheric characterization during the scheduled JWST programs, before concluding in Section 5.

2. Data

2.1. Astrometry and Photometry

TOI-1685 is a magnitude $V = 13.36$ early M dwarf star located in Perseus at a distance $d = 37.596 \pm 0.022$ pc ($\varpi = 26.5893 \pm 0.0192$ mas; Bailer-Jones et al. 2021; Gaia Collaboration et al. 2021). Astrometry and photometry for TOI-1685 are summarized in Table 1. The star's position, proper motion, parallax, and Gaia photometry are drawn from Gaia Data Release 3 (DR3; Gaia Collaboration et al. 2021). Optical photometry on the Gaia system (G, $G_{\rm BP}$, and $G_{\rm RP}$) and synthetic estimates of Johnson B and V and Cousins R_c and I_c are from Gaia DR3, while the TESS synthetic magnitude T is from the TESS Input Catalog (TIC; Stassun et al. 2019). Near-infrared (NIR) J, H, and K_s photometry is adopted from the Two Micron All Sky Survey (2MASS; Cutri et al. 2003).

2.2. TESS Time Series Photometry

TOI-1685 was observed by TESS from UT 2019 November 27 to December 24 at a 2 minute cadence as part of Sector 19 in the TESS primary mission and then again from UT 2022 November 26 to December 23 at a 20 s cadence as part of Guest Observer program 05064[11] in Sector 59.

The Science Processing Operations Center (SPOC) data (Jenkins et al. 2016) for TOI-1685 available at the Mikulski Archive for Space Telescopes website[12] includes both simple aperture photometry (SAP) flux measurements (Twicken et al. 2010; Morris et al. 2017) and presearch data conditioned simple aperture photometry (PDCSAP) flux measurements (Smith et al. 2012; Stumpe et al. 2012, 2014). The instrumental variations present in the SAP flux are removed in the PDCSAP result. At the start of each orbit, thermal effects and strong scattered light impact the systematic error removal in PDC (see TESS data release notes DRN16 and DNR17). Before the fitting process described in Section 3.2, we use the quality flags provided by SPOC to mask out unreliable segments of the time series.

2.3. Ground-based Time Series Photometry

We endeavored to use all publicly available ground-based data of sufficient quality in our transit fit. We started by considering all of the ground-based light curves presented in both B21 and H21, along with previously unpublished

Table 1
Astrometry and Photometry for TOI-1685

Parameter	Value	Source
TIC ID	TIC 28900646	Stassun et al. (2019)
2MASS ID	J04342248+4302148	Cutri et al. (2003)
Gaia DR3 ID	252366608956186240	Gaia DR3
R.A. (hh:mm:ss)[a]	04:34:22.495	Gaia DR3
decl. (dd:mm:ss)	+43:02:14.692	Gaia DR3
μ_α (mas yr^{-1})	37.762 ± 0.022	Gaia DR3
μ_δ (mas yr^{-1})	-87.062 ± 0.018	Gaia DR3
$v_{\rm rad}$ (km s^{-1})	-43.76 ± 0.28	Gaia DR3
Parallax (mas)	26.5893 ± 0.0192	Gaia DR3
Distance (pc)	37.596 ± 0.022	Bailer-Jones et al. (2021)
SpType	M2.65V	Terrien et al. (2015)
B	14.842	Gaia DR3
V	13.362	Gaia DR3
R_c	12.279	Gaia DR3
I_c	10.928	Gaia DR3
G	12.284570 ± 0.002777	Gaia DR3
T (TESS)	11.112 ± 0.007	Stassun et al. (2019)
J	9.616 ± 0.022	Cutri et al. (2003)
H	9.005 ± 0.023	Cutri et al. (2003)
K_s	8.758 ± 0.020	Cutri et al. (2003)
$B - V$ (mag)	1.480	Gaia DR3
$G - K_s$ (mag)	3.527 ± 0.020	Gaia DR3 & Cutri et al. (2003)
$B_p - R_p$ (mag)	2.452011	Gaia DR3
$B_p - G$ (mag)	1.31245	Gaia DR3
$G - R_p$ (mag)	1.139555	Gaia DR3
M_V (mag)	10.486	This work
M_G (mag)	9.408 ± 0.003	This work
M_{Ks} (mag)	5.882 ± 0.020	This work
U (km s^{-1})	35.96 ± 0.19	This work[b]
V (km s^{-1})	-29.97 ± 0.17	This work
W (km s^{-1})	-3.12 ± 0.18	This work

Notes.
[a] Gaia DR3 ICRS R.A. and decl. positions corrected to epoch J2000.0 via Vizier.
[b] Galactic Cartesian velocities (solar system barycentric frame): U, positive toward Galactic center; V, positive toward Galactic rotation; W, positive toward north Galactic pole (following ICRS to Galactic transformations from ESA Special Publication 1997).

[11] "Impacts Of Superflares On TESS Planetary Atmospheres," PI: Ward Howard.

[12] https://mast.stsci.edu

Table 2
Details of the Ground-based Transit Light Curves of TOI-1685 b that We Included in the Transit Analyses Presented in Section 3.2 and the Auxiliary Parameters Used in the Detrending

Date	Instrument	Band	Detrending
2020-02-02	MuSCAT2[a]	r'	am, δx, δy, FWHM
		i'	am, δx, δy, FWHM
		z_s	am, δx, δy, FWHM
2020-03-08	PESTO[b]	i'	am, bg
2020-11-07	Sinistro[c]	i'	am, peak
2020-11-11	Sinistro	i'	am, δy
2020-11-24	MuSCAT[d]	z_s	am, δx, δy, FWHM, peak
2021-01-12	MuSCAT	g'	am, δx, δy, FWHM, peak
		r'	am, δx, δy, FWHM, peak
		z_s	am, δx, δy, FWHM, peak
2021-01-14	MuSCAT	g'	am, δx, δy, FWHM, peak
		z_s	am, δx, δy, FWHM, peak
2021-02-01	MuSCAT3[e]	g'	am, δx, δy, FWHM, peak
		r'	am, δx, δy, FWHM, peak
		i'	am, δx, δy, FWHM, peak
		z_s	am, δx, δy, FWHM, peak
2021-02-02	MuSCAT2	i'	am, δx, δy, FWHM
		z_s	am, δx, δy, FWHM

Note. Auxiliary parameter key: am—air mass; bg—background; δx—x offset; δy—y offset; FWHM —PSF full width at half-maximum; peak—PSF peak brightness. Instrument references: (a) Narita et al. (2019); (b)https://omm-astro.ca/en/instrument/pesto/; (c)https://lco.global/observatory/instruments/sinistro/; (d) Narita et al. (2015); (e) Narita et al. (2020). The full light curves are available in a machine-readable format on Zenodo doi:10.5281/zenodo.11105468.

(This table is available in its entirety in machine-readable form in the online article.)

MuSCAT2 light curves from UT 2020 February 2 and 2021 February 2 (Narita et al. 2019). We discarded all of the MuSCAT2 light curves from UT 2021 January 19 due to poor weather conditions along with the g'- and r'-band MuSCAT2 light curves from UT 2021 January 29 and 2021 February 2 due to saturation of the best comparison star. We performed preliminary fits of the remaining light curves with all parameters except $R_p/R_\star$ fixed to the median values measured from the TESS light curves and discarded light curves where the measured $R_p/R_\star$ was over 4σ from the TESS value. These coincided with light curves particularly affected by time-correlated noise. The light curves that meet these criteria, and which we therefore use in the transit analysis described in Section 3.2, are listed in Table 2 and available via Zenodo at doi:10.5281/zenodo.11105468.

MuSCAT light curves from UT 2020 January 24, 2021 January 10, 2021 January 12, and 2021 January 14 and MuSCAT3 light curves from UT 2021 February 1 were originally presented in H21. MuSCAT2 light curves from UT 2021 January 29 were originally presented in B21.

2.4. Time Series RVs

TOI-1685 was included as a target during the 2020B and 2021B observing semesters on the MAROON-X spectrograph on the Gemini North telescope (Seifahrt et al. 2016, 2018, 2020, 2022). MAROON-X is a stabilized, high-resolution ($R \approx 85{,}000$), fiber-fed echelle spectrograph spanning 500–920 nm that was designed specifically for measuring precision RVs of M dwarf stars. The spectrograph employs two wavelength channels, one in the visible (500–670 nm, abbreviated as MX-Blue) and one in the NIR (650–900 nm, abbreviated as MX-Red). Both channels are exposed simultaneously when observing a target, and each channel produces an independent velocity measurement.

A total of 17 MAROON-X epochs were obtained from 2020 November to December, producing 34 velocity measurements (17 from the MX-Blue arm and 17 from the MX-Red arm). Another 10 MAROON-X epochs were obtained between 2021 October and November, producing 20 velocity measurements (10 observations each from the MX-Blue and MX-Red arms). The MAROON-X velocities are extracted using a customized version of the SERVAL package (Zechmeister et al. 2018) and have the following mean uncertainties: MX-Blue 2020, 1.73 m s^{-1}; MX-Red 2020, 1.02 m s^{-1}; MX-Blue 2021, 1.33 m s^{-1}; MX-Red 2021, 0.77 m s^{-1}.

The star was previously observed using the CARMENES spectrograph on the 3.5 m Calar Alto telescope (Quirrenbach et al. 2014) and the IRD spectrograph on the Subaru telescope (Kotani et al. 2018). The results of these independent RV analyses were published in B21 and H21 for CARMENES and IRD, respectively. Following H21, we discard the IRD data taken on UT 2020 February 2, but all other observations from the three instruments are included in the RV analysis detailed in Section 3.3. The CARMENES data have a mean uncertainty of 2.44 m s^{-1}, while the IRD data have a mean uncertainty of 3.80 m s^{-1}. The time series RVs from all three instruments are presented in an abbreviated form in Table 3 and the full RV data set containing all outputs of the SERVAL pipeline is available as a machine readable table accompanying this publication and on Zenodo at doi:10.5281/zenodo.11105468.

3. Analysis

3.1. Stellar Parameter Analyses

The two exoplanet discovery papers by B21 and H21 differ in the adopted values of the star's estimated metallicity, mass, and radius, all of which impact the conversion of an RV semiamplitude to a planetary mass and a photometric transit depth to a planetary radius. H21 estimated the star's metallicity to be [Fe/H] $= 0.14 \pm 0.12$, its mass to be $M_\star = 0.460 \pm 0.011\ M_\odot$, and its radius to be $R_\star = 0.459 \pm 0.013\ R_\odot$, relying on the parameters from the TIC (Stassun et al. 2019) and the calibration of Mann et al. (2015). B21 estimated the star's metallicity to be [Fe/H] $= -0.13 \pm 0.16$, its mass to be $M_\star = 0.495 \pm 0.019\ M_\odot$, and its radius to be $R_\star = 0.492 \pm 0.015\ R_\odot$ using the M dwarf mass–radius calibration of Schweitzer et al. (2019). We first discuss and try to improve upon the estimation of the star's metallicity before attempting to improve the star's radius and mass.

3.1.1. Color–Magnitude Position and Spectral Type

We plot the star's color–magnitude diagram position ($G - K_s$ versus M_G) in Figure 1. For comparison, we plot the color–magnitude positions for nearby ($d < 25$ pc; $\varpi > 40$ mas) K and M dwarfs from SIMBAD. After removing known white dwarfs, evolved stars, and binaries from the SIMBAD sample, a ninth-order polynomial is fit through the color–magnitude sequence. TOI-1685 sits 0.57 mag above this sequence ($\Delta M_G = -0.57$), which requires an explanation.

Table 3
Combined RV Data Set Used in the Pyaneti Fit Described in Section 3.3

Date [BJD—2450000]	RV ($m\,s^{-1}$)	σ_{RV} ($m\,s^{-1}$)	Inst.	Date (BJD—2450000)	RV ($m\,s^{-1}$)	σ_{RV} ($m\,s^{-1}$)	Inst.	Date (BJD—2450000)	RV ($m\,s^{-1}$)	σ_{RV} ($m\,s^{-1}$)	Inst.
9069.6744	−1.87	2.43	CAR	9153.0232	6.14	3.89	IRD	9184.07505	6.65	1.95	MXB_20
9073.6703	8.05	4.91	CAR	9153.0340	8.67	3.62	IRD	9184.07505	2.52	1.05	MXR_20
9095.6713	−2.74	2.14	CAR	9153.3820	9.91	2.40	CAR	9185.03484	−2.15	1.12	MXB_20
9097.6749	14.20	2.81	CAR	9153.4717	9.87	2.05	CAR	9185.03484	−1.64	0.65	MXR_20
9098.6754	5.97	1.78	CAR	9154.4992	4.88	1.76	CAR	9188.8689	4.06	3.73	IRD
9099.6693	−1.93	2.13	CAR	9154.6201	7.08	1.73	CAR	9188.8796	7.77	5.12	IRD
9101.6859	−0.34	2.63	CAR	9156.4518	1.17	1.60	CAR	9188.9569	−2.30	3.06	IRD
9102.6845	−15.14	3.71	CAR	9156.5853	3.51	1.61	CAR	9188.9711	−0.28	3.46	IRD
9103.6777	1.44	1.84	CAR	9156.9423	−11.49	3.80	IRD	9188.9853	2.51	3.05	IRD
9114.7106	10.09	3.26	CAR	9156.9530	−8.94	3.82	IRD	9189.7977	0.93	3.18	IRD
9118.6966	0.46	2.46	CAR	9157.0269	−10.68	3.84	IRD	9189.8084	−4.72	3.18	IRD
9119.9896	5.20	3.27	IRD	9157.0376	−7.30	3.81	IRD	9189.8678	−6.05	3.13	IRD
9120.0003	7.13	3.66	IRD	9161.3599	8.37	3.26	CAR	9189.8785	−4.89	3.08	IRD
9120.6746	−7.34	1.95	CAR	9161.4505	9.47	3.97	CAR	9242.8903	−2.23	4.10	IRD
9121.6352	−10.46	1.90	CAR	9161.5732	0.63	1.63	CAR	9242.9010	−1.21	4.08	IRD
9122.6841	−0.98	1.82	CAR	9161.6724	−4.24	2.18	CAR	9242.9117	−0.68	4.08	IRD
9123.0154	−2.98	3.11	IRD	9163.3774	5.92	2.99	CAR	9242.9224	0.44	4.23	IRD
9123.0262	−8.46	3.17	IRD	9163.4992	−1.73	3.03	CAR	9242.9330	−4.34	3.77	IRD
9123.0370	−8.64	3.15	IRD	9173.89166	−5.91	1.95	MXB_20	9242.9437	3.64	4.04	IRD
9127.6877	−1.46	2.61	CAR	9173.89166	−2.82	1.19	MXR_20	9244.8374	−5.21	3.99	IRD
9128.6223	2.87	1.83	CAR	9173.98062	−3.88	1.50	MXB_20	9244.8481	−2.10	3.78	IRD
9131.6723	1.86	1.81	CAR	9173.98062	1.55	0.96	MXR_20	9244.8588	−5.52	3.76	IRD
9132.6702	10.82	2.80	CAR	9180.87360	2.30	1.28	MXB_20	9244.9281	1.59	3.76	IRD
9138.6485	5.90	3.33	CAR	9180.87360	1.96	0.82	MXR_20	9244.9388	4.65	3.80	IRD
9139.4464	−5.21	2.91	CAR	9180.95910	−3.00	1.26	MXB_20	9247.7409	−5.18	4.88	IRD
9139.5469	−7.91	1.66	CAR	9180.95910	0.66	0.82	MXR_20	9247.7495	−3.09	4.60	IRD
9139.6241	−4.77	2.93	CAR	9181.03145	−1.31	1.49	MXB_20	9247.7581	−9.92	4.68	IRD
9139.7292	−5.76	1.91	CAR	9181.03145	−3.80	0.90	MXR_20	9247.7667	−11.33	5.29	IRD
9140.5196	−4.64	1.54	CAR	9181.84025	1.50	1.80	MXB_20	9515.03854	−8.55	1.18	MXB_21
9140.5965	−3.62	1.65	CAR	9181.84025	−1.03	1.09	MXR_20	9515.03854	−6.00	0.76	MXR_21
9140.6963	−3.50	1.72	CAR	9181.93144	4.34	1.34	MXB_20	9520.12791	−0.04	1.37	MXB_21
9141.5171	−11.99	2.80	CAR	9181.93144	1.48	0.85	MXR_20	9520.12791	−1.66	0.79	MXR_21
9141.5792	−9.55	2.78	CAR	9182.01259	2.43	2.01	MXB_20	9525.86480	11.91	1.77	MXB_21
9141.6397	−7.51	3.00	CAR	9182.01259	6.32	1.21	MXR_20	9525.86480	14.24	0.97	MXR_21
9141.7027	−8.45	2.59	CAR	9182.81351	6.12	2.15	MXB_20	9529.92016	−2.64	1.38	MXB_21
9142.5187	7.29	2.74	CAR	9182.81351	1.24	1.26	MXR_20	9529.92016	−1.32	0.84	MXR_21
9146.5184	−0.12	2.91	CAR	9182.89216	0.21	1.52	MXB_20	9537.98932	−2.30	1.03	MXB_21
9146.6025	7.18	1.98	CAR	9182.89216	1.05	0.94	MXR_20	9537.98932	0.35	0.65	MXR_21
9147.4080	−3.36	2.12	CAR	9182.97943	−1.90	1.43	MXB_20	9538.85194	0.53	1.28	MXB_21
9147.5126	−5.02	2.86	CAR	9182.97943	−2.50	0.88	MXR_20	9538.85194	−1.10	0.73	MXR_21
9149.4108	−3.60	2.95	CAR	9183.07999	−2.04	2.03	MXB_20	9539.81052	−0.02	1.29	MXB_21
9149.5024	−5.31	2.48	CAR	9183.07999	−3.15	1.09	MXR_20	9539.81052	−4.02	0.64	MXR_21
9149.5915	−6.27	2.76	CAR	9183.76783	0.54	2.26	MXB_20	9539.85581	0.14	1.08	MXB_21
9149.6962	−3.53	3.95	CAR	9183.76783	0.84	1.10	MXR_20	9539.85581	−0.46	0.62	MXR_21
9150.3895	−5.06	2.30	CAR	9183.83016	3.20	2.87	MXB_20	9539.99341	6.26	1.54	MXB_21
9151.6239	0.51	1.78	CAR	9183.83016	−3.87	1.63	MXR_20	9539.99341	4.67	0.91	MXR_21
9151.7309	10.76	1.97	CAR	9183.99424	2.76	1.52	MXB_20	9540.05145	4.77	1.41	MXB_21
9152.4645	7.73	1.74	CAR	9183.99424	2.50	0.90	MXR_20	9540.05145	5.44	0.79	MXR_21

Note. A machine-readable version of this table is available, including a version with all SERVAL fit parameters. Instruments include CARMENES (CAR) and IRD, both of which observed the star over a single semester in 2020, and MAROON-X, which observed the star across two semesters in 2020 and 2021. The MAROON-X instrument labels contain information on which detector the RV is derived from (Blue or Red, represented as B and R) and in which year the observation was taken (2020 or 2021), as each combination is treated as a separate instrument in the RV fit.

(This table is available in its entirety in machine-readable form in the online article.)

The null results of the high-resolution imaging presented in the B21 and H21 papers, the lack of any long-term RV trend, and the star's low Gaia DR3 RUWE value (RUWE = 1.179) suggests that the star lacks an unresolved stellar companion,[13] hinting that the star must be either metal-rich or pre-main-sequence (e.g., Johnson & Apps 2009; Bell et al. 2015) or be subject to significant stellar reddening.

Stellar reddening can be ruled out, as both the B21 and H21 spectroscopic analyses show that the star is indeed an early M dwarf whose effective temperature and color estimates are consistent, and at $d = 37.6$ pc (Bailer-Jones et al. 2021), the star

[13] RUWE > 1.4 is typically considered a signal of unresolved stellar multiplicity (Lindegren et al. 2021).

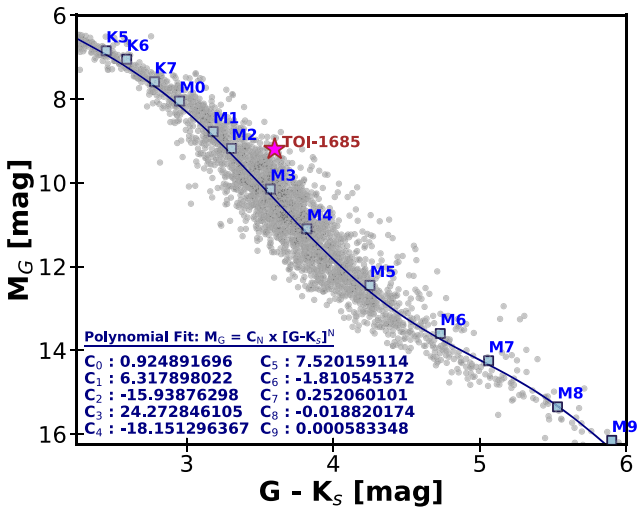

Figure 1. Color–magnitude diagram ($G - K_s$ vs. M_G, with the G magnitude taken from Gaia Collaboration et al. 2021 and the 2MASS K_s magnitude from Cutri et al. 2003) for stars within 25 pc ($\varpi > 40$ mas) in SIMBAD, subtracting known white dwarfs, binary stars, and giants. The vast majority of the fiducial values for parallax ϖ and magnitudes G and K_s in SIMBAD come from Gaia DR3 for the first two and 2MASS for the latter. The blue line is a ninth-order polynomial fit, with spectral types labeled at their mean colors from the updated online table from Pecaut & Mamajek (2013). TOI-1685, depicted as a pink star, is 0.57 mag brighter than the main-sequence locus.

is well within the Local Bubble, where reddening should be negligible (Reis et al. 2011; Lallement et al. 2018). Further, there are no indications that the star could be pre-main-sequence. TOI-1685 is slow-rotating ($v \sin i < 2.0$ km s^{-1}; Marfil et al. 2021) and relatively inactive, and its relatively high space velocity ($S_{\rm tot} = 47$ km s^{-1}) is not consistent with membership in any of <100 pc young moving groups or clusters (using BANYAN Σ; Gagné et al. 2018). Hence, we interpret the star's overluminosity in color–magnitude space as an indicator of high metallicity.

The spectral subtype for TOI-1685 has been variously quoted as M1 (Bai et al. 2018), M2 (Lu et al. 2019; Xiang et al. 2019), M2.3 ± 0.5 (Sebastian et al. 2021), M2.4 (Birky et al. 2020), M2.5 (Zhong et al. 2015), M2.65 (Terrien et al. 2015), M3.0 (Zhong et al. 2015), and M3.02 (Terrien et al. 2015). Through comparison of the broadband visible and NIR absolute magnitudes of TOI-1685 (those of Kirkpatrick et al. 1991) to M dwarf standard stars using the 2MASS photometry, Gaia DR3 photometry, and astrometry compiled in SIMBAD (Wenger et al. 2000; Cutri et al. 2003; Gaia Collaboration et al. 2021), we find that TOI-1685 is most similar to three M2.5V standard stars: TOI-1685 ($G - K_s = 3.53$, $M_G = 9.41$, $M_{Ks} = 5.88$), GJ 381[14] ($G - K_s = 3.42$, $M_G = 9.30$, $M_{Ks} = 5.88$), GJ 767B ($G - K_s = 3.65$, $M_G = 9.41$, $M_{Ks} = 5.76$), and GJ 250B ($G - K_s = 3.37$, $M_G = 9.39$, $M_{Ks} = 6.01$). So the absolute photometry for TOI-1685 is at least consistent with a spectral type of approximately M2.5V, similar to that quoted by Terrien et al. (2015), Zhong et al. (2015), and Sebastian et al. (2021).

3.1.2. Stellar Metallicity

There are several published metallicity estimates for TOI-1685, which are summarized in Table 4. These range from −0.22 to +0.22, with numerous entries in between. Safe to say, the metallicity for the star seems to be poorly constrained, other than that it is likely within a couple tenths of a dex of solar. We therefore proceed to generate an independent photometric metallicity estimate of this star.

After the pioneering attempts by Bonfils et al. (2005) to estimate photometric metallicities for M dwarfs using VK_s color–absolute magnitude relations, multiple studies have attempted to improve their accuracy (see, e.g., Johnson & Apps 2009; Schlaufman & Laughlin 2010; Neves et al. 2013). All of the calibrations connect M dwarf companions to FGK-type primary stars with measured metallicities. We list the photometric metallicity estimates using these four calibrations in Table 4 for reference.

Using the calibration of Johnson & Apps (2009) and adopting the values $V = 13.362$, $K_s = 8.758$, and $M_{Ks} = 5.882$ (Table 1), we find that TOI-1685 is 0.70 mag above their M dwarf main sequence in $(V - K_s)$ versus M_{Ks} space and estimate a photometric metallicity of [Fe/H] = +0.34. Using the calibration of Schlaufman & Laughlin (2010), we find that the star's colors are significantly red for its absolute magnitude ($\Delta(V - K_s) = 0.45$), consistent with a photometric metallicity of [Fe/H] = +0.19. We note that both the Schlaufman & Laughlin (2010) and Neves et al. (2013) calibrations adopt a mean metallicity for field M dwarfs that is somewhat low ([Fe/H] = −0.17).

Using the recent PASTEL compiled catalog of metallicities from Soubiran et al. (2022), we find that the local G and K dwarfs in SIMBAD with distances of $d < 25$ pc ($\varpi > 40$ mas) and dwarflike surface gravities ($4 < \log g < 5$) are consistent with having distributions of metallicities [Fe/H] with means, standard errors, and standard deviations of ([Fe/H] = −0.06 ± 0.01, $\sigma = 0.21$ dex; N(G dwarf) = 216) and ([Fe/H] = −0.05 ± 0.01, $\sigma = 0.23$ dex; N(K dwarf) = 282), respectively.

These distributions are immune to outliers, as they are the averages of three estimates of the mean μ (median, Chauvenet-clipped mean, and probit mean), two estimates of the standard error σ_μ (error of the true median and standard error of the Chauvenet-clipped mean), and two estimates of the standard deviation σ (68% confidence intervals and probit estimate of standard deviation).[15] Only a handful of metal-poor stars were clipped from these distributions following Chauvenet's criterion (Bevington & Robinson 1992): three G dwarfs with metallicities between −0.88 and −0.83 and six K dwarfs with metallicities between −1.76 and −1.04, which are likely halo stars. Hence, the distribution of metallicities [Fe/H] for the local G and K dwarfs within $d < 25$ pc is nearly identical.

K dwarfs are similar to the M dwarfs in that we do not expect them to have evolved off the main sequence during the Galaxy's lifetime. The main-sequence lifetime for a ∼0.86 $M_\odot$ K0V star is ∼20 Gyr, i.e., older than the Universe, and the lifetimes for lower-mass stars are even longer. Therefore, we expect the local main-sequence K and M dwarfs to have similar metallicity distributions (e.g., Johnson & Apps 2009).

If we reevaluate the Schlaufman & Laughlin (2010) calibration using the updated PASTEL adopted mean field dwarf metallicity of [Fe/H] = −0.05 for K dwarfs, one would derive a new photometric metallicity estimate for TOI-1685 of [Fe/H] = +0.31. This is almost identical to the estimate that we derived using the Johnson & Apps (2009) calibration and just slightly higher than the recent value published in H21

[14] A tight binary (∼0.″2) unresolved in Gaia or 2MASS (Mann et al. 2019).

[15] For detailed discussions of these statistical estimators, see Lutz & Upgren (1980), Bevington & Robinson (1992), and Gott et al. (2001).

Table 4
Stellar Parameter Estimates for TOI-1685

Published Literature Values								
Param.	Value	Reference	Param.	Value	Reference	Param.	Value	Reference
Fe/H	-0.13 ± 0.16	B21	$M_\star$	0.495 ± 0.019	B21	$R_\star$	0.492 ± 0.015	B21
Fe/H	$+0.14 \pm 0.12$	H21	$M_\star$	0.460 ± 0.011	H21	$R_\star$	0.459 ± 0.013	H21
Fe/H	-0.20	Ding et al. (2022) (a)	$M_\star$	0.4600 ± 0.020	Stassun et al. (2019)	$R_\star$	0.462 ± 0.014	Stassun et al. (2019)
Fe/H	-0.18	Ding et al. (2022) (a)	$M_\star$	0.46 ± 0.01	Sebastian et al. (2021)		...	...
Fe/H	-0.064 ± 0.008	Sprague et al. (2022)	$M_\star$	$0.461^{+0.003}_{-0.018}$	Morrell & Naylor (2019)		...	...
Fe/H	-0.05 ± 0.05	Yu et al. (2023)	$M_\star$	0.4999 ± 0.00044	Queiroz et al. (2020)		...	...
M/H	-0.01	Sarmento et al. (2021)	$M_\star$	0.47	Kervella et al. (2022)		...	...
Fe/H	-0.01	Terrien et al. (2015) (b)	$M_\star$	0.573 ± 0.045	Muirhead et al. (2018)		...	...
Fe/H	$+0.08$	Terrien et al. (2015) (c)		...	...		...	...
Fe/H	$+0.22$	Terrien et al. (2015) (d)		...	...		...	...
Values Derived in This Work								
Param.	Value	Reference	Param.	Value	Reference	Param.	Value	Reference
Fe/H	$+0.04$	This work (e)	$M_\star$	0.454 ± 0.018	This work	$R_\star$	0.4555 ± 0.0128	This work
Fe/H	$+0.34$	This work (f)		...	...		...	...
Fe/H	$+0.19$	This work (g)		...	...		...	...
Fe/H	$+0.09$	This work (h)		...	...		...	...
Adopted Values								
Fe/H	$+0.3 \pm 0.1$	This work	$M_\star$	0.454 ± 0.018	This work	$R_\star$	0.4555 ± 0.0128	This work

Note. (a) Fe/H measurements from two different LAMOST spectra; (b) H band; (c) J band; (d) K_s band; (e) this work, photometric metallicity calculated using Bonfils et al. (2005) calibration; (f) this work, photometric metallicity using Johnson & Apps (2009) calibration; (g) this work, photometric metallicity using Schlaufman & Laughlin (2010) calibration; (h) this work, photometric metallicity using Neves et al. (2013) calibration.

([Fe/H] $= +0.27 \pm 0.12$ dex), which analyzed IRD spectra using measurements of atomic lines and comparing them to synthetic M dwarf spectra.

As a check on the plausibility of such a high metallicity for TOI-1685, we reexamined the trend for spectroscopic metallicities for the metal-rich primaries of stars with M dwarf companions in Table 1 of Johnson & Apps (2009). Their subsample of metal-rich M dwarfs includes the stars HD 46375 B, HD 38529 B, HD 18143 C, 55 Cnc B, HD 190360 B, and Proxima Centauri, which had ΔM_{Ks} offsets above the main sequence of 0.48, 0.67, 0.68, 0.67, 0.43, and 0.36 mag, respectively.

Querying the recent PASTEL compilation of [Fe/H] values from Soubiran et al. (2022), we find that the metallicities of the primary FGK stars for these M dwarfs had [Fe/H] values of 0.24 ± 0.01, 0.34 ± 0.01, 0.18 ± 0.05, 0.32 ± 0.02, 0.22 ± 0.01, and 0.22 (adopting the mean for α Cen A and B), respectively. Indeed, after clipping the pair for HD 18143 C with the largest metallicity uncertainty ($\Delta M_{Ks} = 0.68$, [Fe/H] $= 0.18 \pm 0.05$), the correlation between ΔM_{Ks} and [Fe/H] becomes remarkably tight ($\sigma_{\rm [Fe/H]} = 0.016$ dex) for the remaining five stars:

$$[\mathrm{Fe/H}] = 0.062 + 0.395 \Delta M_{Ks} \quad (1)$$

in the limited range 0.36 mag $< \Delta M_{Ks} <$ 0.67 mag. Using the Johnson & Apps (2009) $V - K_s$ versus M_{Ks} calibration, TOI-1685 has $\Delta M_{Ks} = 0.70$ mag, which is slightly more luminous than even this limited sample of very metal-rich stars examined in the 2009 paper. Extrapolating this trend to the negligibly more luminous ΔM_{Ks} of 0.70 mag would predict a metallicity of [Fe/H] $= +0.34 \pm 0.02$, i.e., comparable to the other extremely metal-rich M dwarfs HD 38529 B (M2.5V, $V - K_s = 4.55$, $M_{Ks} = 5.66$, $\Delta M_{Ks} = 0.67$, [Fe/H] $= +0.34 \pm 0.01$) and 55 Cnc B (M4V, $V - K_s = 5.48$, M_{Ks}=7.21, ΔM_{Ks}=0.67, [Fe/H] $= +0.32 \pm 0.02$).

We discount other measurements that measure values closer to solar, as the color–magnitude position of the star is extremely well measured, and none of the explanations for the star's overluminosity (~0.7 mag) above the color–magnitude locus for field M dwarfs makes sense with lower metallicities.

Taking into account our photometric metallicity estimates and the value from H21, we adopt a final metallicity value [Fe/H] $= +0.3 \pm 0.1$.

3.1.3. Stellar Mass

We can now estimate the star's mass via the Mann et al. (2019) absolute magnitude–mass–metallicity calibration using the star's adopted parameters ($K_s = 8.758 \pm 0.020$, $\varpi = 26.5893 \pm 0.0192$ mas, [Fe/H] $= +0.3 \pm 0.1$, $A_V = 0$), which results in a final mass estimate of $M_\star = 0.454 \pm 0.018\ M_\odot$ (3.9% uncertainty). This estimate is 1.3% smaller than the stellar mass in H21 and 9.0% smaller than the stellar mass in B21 (Table 4). The agreement between our value and that from H21 is unsurprising,

as both rely on the Mann et al. (2019) calibrations, and the final H21 stellar metallicity estimate was also somewhat metal-rich ($+0.14 \pm 0.12$), whereas the value from B21 was calculated using an estimated radius and a radius–mass calibration from Schweitzer et al. (2019) based on eclipsing binary stars.

3.1.4. Stellar Radius

Previously published radius estimates for TOI-1685 are listed in Table 4. We estimate the radius of TOI-1685 using the empirical absolute magnitude–metallicity–radius calibration of Mann et al. (2015). Adopting $M_{Ks} = 5.882 \pm 0.020$ and [Fe/H] $= +0.3 \pm 0.1$, the Mann et al. (2015) calibration estimates a radius of $R_\star = 0.4555 \pm 0.0128\ R_\odot$. We estimate the radius uncertainty (2.8%) using the quadrature sum of 0.8% from the uncertainties in the absolute magnitude and metallicity and 2.7% from the rms scatter in the Mann et al. (2015) calibration. This estimate is 0.8% smaller than the stellar radius in H21 and 8.0% smaller than the stellar radius in B21.

3.1.5. Bolometric Flux, Luminosity, and Effective Temperature

We estimate the stellar bolometric flux and luminosity through analysis of the spectral energy distributions (SEDs) using two independent codes: the Virtual Observatory SED Analyzer[16] (VOSA; Bayo et al. 2008) and the spectrAl eneRgy dIstribution bAyesian moDel averagiNg fittEr[17] (ARIADNE; Vines & Jenkins 2022). We then combine the estimated luminosity with the empirical radius estimate from Section 3.1.4 to calculate an independent effective temperature.

The VOSA online tool queries databases of photometry and fits synthetic stellar spectra of varying parameters (e.g., $T_{\rm eff}$, log g, [Fe/H]) from different published spectral libraries while accounting for user-defined distance and reddening (Bayo et al. 2008). The VOSA query for TOI-1685 yielded 111 published photometric measurements within 5″ of the J2000 position of the star, between 0.36μm and 22μm. We initially omit from further analysis several magnitudes that were very discrepant at the >1 mag level: z and y from Pan-STARRS PS1 and J, H, and K (two K mags) from UKIDSS. The vast majority of the remaining VOSA magnitudes are "OAJ" and "JPAS" values—magnitudes synthesized from spectrophotometrically calibrated Gaia DR3 Bp/Rp spectra (Montegriffo et al. 2023) on the photometric system of the Observatorio Astrofísico de Javalambre (OAJ) surveys Javalambre Physics of the Accelerating Universe Astrophysical Survey (J-PAS; Benitez et al. 2014)[18] and Javalambre-Photometric Local Universe Survey (J-PLUS; Cenarro et al. 2019).[19] Additional data include measured photometry from Gaia DR3 (Gaia Collaboration et al. 2021), APASS (Henden et al. 2016), 2MASS (Cutri et al. 2003), Wide-field Infrared Survey Explorer (WISE; Cutri et al. 2012), and NEOWISE (Mainzer et al. 2011). Given the dense coverage of the OAJ and J-PAS photometry based on Gaia DR3 spectrophotometry, we omit several of the synthetic broadband magnitudes that duplicate coverage (e.g., Johnson *BVRI*; Sloan Digital Sky Survey, SDSS, *griz*; HST/Advanced Camera for Surveys/WFC F606W and F814W; and Pan-STARRS y). Despite it defining the blue end of the photometric coverage, we also omitted the synthetic SDSS u photometry from Gaia DR3 from the analysis, as the synthetic photometry for wavelengths shorter than 400 nm may contain systematic errors (Montegriffo et al. 2023).

For fitting the SEDs, we adopted zero extinction ($A_V = 0$), a reasonable assumption as, at ∼38 pc, TOI-1685 is within the Local Bubble (e.g., Reis et al. 2011), and modern 3D reddening maps like STILISM (Lallement et al. 2018) predict negligible reddening ($E(B-V) = 0.001 \pm 0.014$ mag) at $d = 35-40$ pc. We used VOSA to fit multiple grids of synthetic stellar spectral models (e.g., BT-Settl, BT-Settl/AGSS2009, BT-Settl/CIFIST, BT-Settl/GNS93, BT-Cond, BT-Dusty, BT-NextGen/AGSS2009, BT-NextGen/GNS93) over a range of stellar temperature and gravity appropriate for main-sequence M dwarf stars (2300 K < $T_{\rm eff}$ < 3900 K; 4.5 < log g < 5.0) and sample over the full range of metallicities covered by the models (although some only used solar). The best-fit model to the SED of TOI-1685 was a BT-Settl model (Allard et al. 2013) with CIFIST2011 solar abundances (Caffau et al. 2011) that resulted in $T_{\rm eff} = 3400 \pm 50$ K, log g $= 5.00 \pm 0.25$, [M/H] $= 0.0$ (constrained), with bolometric flux $f_{\rm bol} = (6.90408 \pm 0.00048) \times 10^{-10}$ erg s^{-1} cm^{-2}, or $m_{\rm bol} = 11.404750 \pm 0.000075$ on the IAU 2015 bolometric flux/magnitude scale (Mamajek et al. 2015; Figure 2). This resulted in a stellar bolometric luminosity of $L = 0.030524$ $L_\odot$ (±0.15%) or $\log(L/L_\odot) = -1.51537 \pm 0.00065$ dex. The fit used 87 of the 90 data points, and the relative uncertainty in the flux is fantastically tiny (0.0049%), much smaller than the absolute uncertainties achievable in spectrophotometry.

The best-calibrated spectrophotometric standard stars are absolutely flux-calibrated in the visible and NIR to ∼1% (e.g., Bohlin et al. 2019; Rieke et al. 2022), and photometric passband zero-point fluxes for the classic visible and NIR bands (e.g., Johnson, 2MASS, etc.; Mann & von Braun 2015), Gaia photometry (Pancino et al. 2021), and Gaia synthetic photometry (Pancino et al. 2022) all appear to be accurate at the ∼1% level. Considering that the absolute flux calibration of the SED fit includes uncertainties from all of these sources, we conservatively adopt an $f_{\rm bol}$ uncertainty of 2%, or $f_{\rm bol} = (6.904 \pm 0.138) \times 10^{-10}$ erg s^{-1} cm^{-2} and $m_{\rm bol} = 11.405 \pm 0.022$ on the IAU 2015 bolometric flux/magnitude scale (Mamajek et al. 2015). This results in a stellar bolometric luminosity of $L = 0.03052 \pm 0.00061$ $L_\odot$ or $\log(L/L_\odot) = -1.51537 \pm 0.00869$ dex.

`ARIADNE` uses Bayesian model averaging to include information from a variety of stellar models (e.g., BT-Settl, BT-Cond, BT-NextGen, and Phoenix) when determining the best-fit stellar $T_{\rm eff}$, log g, [Fe/H], and radius. The package's built-in search function returns a smaller set of photometry than VOSA, consisting of the Gaia $B_{\rm P}$, G, and $R_{\rm P}$ bands; 2MASS J, H, and $K_{\rm s}$ bands; and WISE W1 and W2 bands. The Bayesian fit of the SEDs to the photometry, with the extinction again fixed to 0, is $T_{\rm eff} = 3431^{+83}_{-42}$ K, log $g = 4.83^{+0.043}_{-0.039}$ dex, [Fe/H] $= 0.26^{+0.16}_{-0.19}$, and $R_\star = 0.4838^{+0.0173}_{-0.0185}\ R_\odot$. The corresponding best-fit luminosity is $0.02922^{+0.0034}_{-0.0026}\ L_\odot$, which is 4.3% (2.2$\sigma$) lower than the VOSA estimate above. The BT-Settl model is preferred over the Phoenix model in a 69% to 31% probability ratio.

Through fitting a NextGen model to 10 broadband photometry data points, H21 estimated $f_{\rm bol} = (6.65 \pm 0.15) \times 10^{-10}$ erg s^{-1} cm^{-2} ($m_{\rm bol} = 11.445 \pm 0.024$ mag on IAU scale) and $L_{\rm bol} = 0.0271^{+0.0028}_{-0.0026}\ L_\odot$(their Table 1). The luminosity for TOI-1685 quoted by H21 in their Table 1 is notably 11.2%

[16] http://svo2.cab.inta-csic.es/theory/vosa/
[17] https://github.com/jvines/astroARIADNE
[18] https://www.j-pas.org/survey
[19] https://www.j-plus.es/

Table 5
Effective Temperature Estimates for TOI-1685

Value	Reference	Value	Reference
		Published Literature Values	
3434 ± 51 K	B21	3660 ± 9 K	Olney et al. (2020)
3428 ± 97 K	H21 (a)	3450 K	Morrell & Naylor (2019)
3475 ± 75 K	H21 (b)	3457 ± 157 K	Stassun et al. (2019)
3429 ± 114 K	Hardegree-Ullman et al. (2023)	3463^{+24}_{-29} K	Anders et al. (2019)
3612 ± 98 K	Yu et al. (2023)	3986 ± 33 K	Xiang et al. (2019) (h)
3594 ± 10 K	Sprague et al. (2022)	4165 ± 47 K	Xiang et al. (2019) (h)
3629 ± 105 K	Sebastian et al. (2021)	3490 ± 63 K	Muirhead et al. (2018)
3504 K	Birky et al. (2020) (c)	3624 K	Bai et al. (2018)
3615 ± 157 K	Zhang et al. (2020) (d)	3473 K	Terrien et al. (2015) (i)
3579 ± 138 K	Zhang et al. (2020) (e)	3481 K	Terrien et al. (2015) (j)
3596^{+9}_{-11} K	Queiroz et al. (2020)	3499 K	Terrien et al. (2015) (k)
3600 K	Jönsson et al. (2020) (f)	3555 K	Terrien et al. (2015) (l)
3688 ± 60 K	Jönsson et al. (2020) (g)	3888^{+202}_{-417} K	Gaia DR2
		Values Derived in This Work	
3575 ± 53 K	This work (m), adopted	3431^{+83}_{-42} K	This work (n)

Note. For papers that contain more than one method for estimating $T_{\rm eff}$, we use the following notes to clarify which value is reported in this table: (a) H21 IRD spectrum analysis; (b) H21 NextGen SED analysis; (c) Birky et al. (2020) ASPCAP pipeline; (d) Zhang et al. (2020) first APOGEE/SLAM fit, but it gives unrealistically low gravity ($\log g \sim 1$) and metallicity ([M/H] ~ -0.9); (e) Zhang et al. (2020) second APOGEE/SLAM fit, but it gives unrealistically low gravity ($\log g \sim 1.2$) and metallicity ([M/H] ~ -0.5); (f) Jönsson et al. (2020) APOGEE-2; (g) Jönsson et al. (2020) APOGEE-2/ASPCAP; (h) Xiang et al. (2019) estimates from two independent spectra, but the fits give unrealistic gravity and metallicity ($\log g \simeq 4$ and [Fe/H] $\simeq -1.4$); (i) Terrien et al. (2015) K-index; (j) Newton et al. (2015); Terrien et al. (2015) calibration; (k) Terrien et al. (2015) H-index; (l) Terrien et al. (2015) J-index; (m) derived from VOSA luminosity estimate combined with updated empirical radius estimate from Mann et al. (2015); (n) ARIADNE SED fit results.

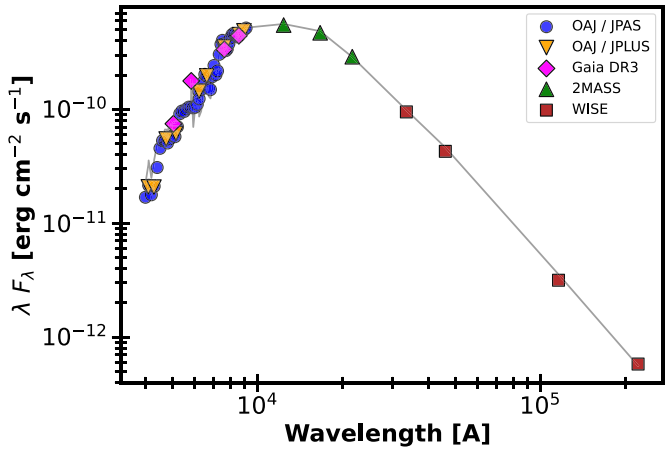

Figure 2. Best-fit SED for TOI-1685 from VOSA. Colored points are photometric magnitudes from the Gaia, 2MASS, and WISE surveys and magnitudes synthesized from spectrophotometrically calibrated Gaia DR3 Bp/Rp spectra into the photometric system of the OAJ J-PAS and J-PLUS. The gray line depicts the model flux measurements.

lower than what we estimate and at 3.7σ relative to the uncertainties we and they quote in $L_{\rm bol}$. Oddly, if one combines the Gaia DR3 distance (37.609 pc) and $f_{\rm bol}$ in H21's Table 1 through $L = 4\pi d^2 f_{\rm bol}$, one would estimate a stellar luminosity of $L_{\rm bol} = 0.0294\ L_\odot$, remarkably 8.5% higher than the luminosity quoted in their Table 1 and only 3.7% lower than our estimated luminosity from the VOSA SED fit. We conclude that the luminosity for TOI-1685 in H21 is likely underestimated by $\sim$11%, and that the actual agreement in $f_{\rm bol}$ and $L_{\rm bol}$ estimates between our VOSA SED analysis and the NextGen SED fit from H21 is actually at the $\sim 3.7 \pm 3.0\%$ (1.2σ) level, i.e., consistent.

Combining our new luminosity estimate ($L = 0.03052 \pm 0.00061\ L_\odot$) with the empirical radius estimate derived in Section 3.1.4 ($R_\star = 0.4555 \pm 0.0128\ R_\odot$), we derive an independent effective temperature that we adopt for the rest of the Letter's analyses and discussions: $T_{\rm eff} = 3575 \pm 53$ K. This value is within 150 K of the value derived from the ARIADNE SED analysis. Table 5 summarizes previously published $T_{\rm eff}$ estimates for TOI-1685, and the values span nearly 20%. The median of these previously published estimates is $T_{\rm eff} = 3502$ K, just 1.4σ lower than our new VOSA-based value. Further, our new estimate is within 2σ of several published estimates (Terrien et al. 2015; Bai et al. 2018; Muirhead et al. 2018; Birky et al. 2020; Jönsson et al. 2020; Queiroz et al. 2020; H21; Sebastian et al. 2021; Sprague et al. 2022; Yu et al. 2023) based on multiple methods (analysis of visible or NIR spectra, SED fits, color–$T_{\rm eff}$ relations).

3.1.6. Stellar Rotation and Age

Our best-fit RV analysis of TOI-1685 yielded a quasiperiodic signal with a period posterior distribution of 18.2 ± 0.5 days, similar to the 19 day signal observed in B21. We interpret this to represent the rotation of the star.

Main-sequence dwarf stars spin down by losing angular momentum through a magnetized wind, and under certain conditions, a rotation period can be used to estimate the star's gyrochronologic age. Namely, if it has spun down sufficiently such that the Rossby number (ratio of rotation period to convective turnover time) is larger than a critical value, its magnetic activity is below the "saturation" level, and a rotation-dependent braking law erases differences in initial spin rates and causes convergence to a single temperature-dependent rotation sequence. Models are not advanced enough to produce robust braking laws applicable to different stellar types, and

empirical calibration using observed rotation sequences at appropriate ages is needed. Germane to TOI-1685, Dungee et al. (2022) established a rotation sequence for early-type M dwarfs in the 4 Gyr old cluster M67. Combining this with younger sequences (e.g., Curtis et al. 2020), Gaidos et al. (2023) assigned ages with formal uncertainties to the late K and early M-type host stars of many known exoplanets. The primary sources of error are uncertainties in rotation period and $T_{\rm eff}$, residual star-to-star differences in spin, and the effect of metallicity (which affects the moment of inertia and also perhaps the braking law).[20] Using the procedures described in Gaidos et al. (2023), we estimate an age of 1.0 ± 0.3 Gyr for TOI-1685, with a model-based correction for $[{\rm Fe/H}] = +0.3$ of 0.3 Gyr (i.e., the star's actual age could be $\sim$1.3 Gyr; see Figure 5 in Gaidos et al. 2023).

3.2. Transit Photometry Analyses

To jointly model all of the TESS data (see Section 2.2) and various ground-based photometric light curves (see Section 2.3), we used the sum of components modeling the transit of TOI-1685 b, quasiperiodic modulations arising due to stellar activity, and systematic noise originating in each instrument. To achieve this, we used `juliet` (Espinoza et al. 2019), a python package that facilities the simultaneous modeling of transit data acquired in multiple bandpasses.

For the transit, we used a Mandel & Agol (2002) transit model generated using the `batman` package (Kreidberg 2015) and parameterized using the period P, transit time t_0, radius ratio $R_{\rm p}/R_\star$, impact parameter b, and stellar density $\rho_\star$, with eccentricity e fixed to 0. We used the quadratic law to model limb darkening, following the q parameterization of Kipping (2013). Different light curves acquired using a common bandpass (see "Band" column in Table 2) shared a single pair of limb-darkening coefficients.

For each of the ground-based light curves, we included auxiliary observing parameters such as air mass and detector $x - y$ offset in the model to decorrelate systematic noise, with the parameters used for each light curve shown by the "Detrending" column in Table 2.

Quasiperiodic photometric variability with a timescale of a few days was apparent by eye in both TESS sectors, in line with expectations for stellar variability of early M-type stars. However, both the period and amplitude of the variability change significantly in the intervening 2 yr between the two TESS sectors. The Lomb–Scargle periodogram indicated a 10 day periodicity that was present in both sectors, along with a 4.5 day periodicity that was only present in Sector 59. For this reason, we used two different Gaussian processes (GPs; Gibson 2014) using a simple harmonic oscillator kernel generated using the `celerite` package (Foreman-Mackey et al. 2017) with quality factor Q—which dictates the coherency of the oscillations—set to $1/\sqrt{2}$. The first GP was designed to fit the 10 day periodicity that was relatively consistent in both sectors, while the second GP fit only the additional 4.5 day periodicity in Sector 59.

There was residual time-correlated noise on timescales longer than the observations in many of the ground-based light curves even after detrending against the auxiliary observing parameters, likely originating from the same stellar variability. We tested fitting GPs with a range of periods covering those that we observed in both sectors of TESS data to the ground-based light curves and found them to be broadly consistent with all of them, mainly due to the limited time baseline of the light curves. As both GPs used to fit the TESS data described the residual noise in the ground-based light curves well, and to avoid adding unnecessary extra degrees of freedom to the baseline models of the ground-based light curves, we extended the 10 day GP described in the paragraph above to jointly model the variability in all of the ground-based light curves as well.

To derive the joint posterior distributions for each free parameter, we used the Dynamic Nested Sampler (see Skilling 2004, 2006; Higson et al. 2019) from the `dynesty` package (Speagle 2020). We used the new measurements of the stellar mass and radius presented, respectively, in Sections 3.1.3 and 3.1.4 to place a Gaussian prior on $\rho_\star$. As Patel & Espinoza (2022) found a significant discrepancy between theoretically predicted and empirical limb-darkening coefficients for M dwarfs, we selected uniform priors that allowed all physically possible values to be sampled (i.e., with limits at 0 and 1). We placed wide uniform priors on P, t_0, $R_{\rm p}/R_\star$, b, and the linear coefficients of the auxiliary observing parameters, along with wide uniform priors on the logarithm of the GP hyperparameters. The results for a selection of transit and physical parameters are displayed in Table 6, with the other free parameters displayed in Table A1 of the Appendix. The final best-fit transit depth is $\Delta F = 874^{+34}_{-36}$ ppm, which is 14.4% smaller than the 1 ppt depth measured by H21 and B21 (Figure 3).

Combining the updated stellar radius estimate of $R_\star = 0.4555 \pm 0.0128\ R_\odot$ with our best-fit transit depth produces an updated planet radius measurement of $1.468 \pm 0.05\ R_\oplus$ for TOI-1685 b.

3.3. RV Analyses

To jointly model the combined CARMENES, IRD, MAROON-X Blue, and MAROON-X Red data sets, we used Pyaneti (Barragán et al. 2019, 2022), an open-source python package. Pyaneti can perform traditional 1D GP fits, multidimensional GP fits, and floating chunk offset fits (Hatzes et al. 2011).

One current restriction of Pyaneti is that RV data sets must be square matrices, meaning that each instrument must have the same input columns (date, RV, RV error, activity index, etc). While the CARMENES and MAROON-X data sets both produce estimates of the differential line width (dLW) of the RV spectra and spectral activity indicators derived using the Hα and calcium IR triplet absorption lines, the IRD data set does not contain any overlapping activity indices. Therefore, opting for a multidimensional GP model would require removing the IRD data from the fit.

To assess this option, we performed a series of 2D GP fits that incorporate just the MAROON-X and CARMENES data sets, first using the RVs and the dLW time series, then the RVs and the Hα time series, and finally the RVs and the Ca IR triplet time series. We find that the dLW measurements are not informative enough to further constrain the GP, as they exhibit significant scatter around the best-fit model. RV instruments and data reduction pipelines are built to be most sensitive to the centroids of absorption lines (used to measure the star's RV) rather than to asymmetries in the lines' shapes (captured in the

[20] The metallicity of M67 and the young clusters used to construct the gyrochronology in Gaidos et al. (2023) are all close to solar.

Table 6
Selection of the Updated Stellar and System Parameters from the Stellar Characterization Described in Section 3.1, the Transit Photometry Fit Described in Section 3.2, and the 1D GP RV Fit Described in Section 3.3

Parameter		Adopted Value	Comparison[a] to B21	Comparison to H21
Adopted Stellar Parameters				
Stellar metallicity [Fe/H]	...	0.3 ± 0.1	↑ 143%	↑ 53%
Stellar radius [$R_\odot$]	...	0.4555 ± 0.0128	↓ 8.0%	↓ 0.8%
Stellar mass [$M_\odot$]	...	0.454 ± 0.018	↓ 9.0%	↓ 1.3%
Stellar F_{bol} [erg s^{-1} cm^{-2}]	...	$(6.904 \pm 0.138) \times 10^{-10}$	NR[b]	↑ 3.7%
Stellar luminosity [$L_\odot$]	...	0.03052 ± 0.00061	↑ 0.7%	↑ 3.7 / ↑ 11.2%[c]
Stellar T_{eff} [K]	...	3575 ± 53	↑ 3.9%	↑ 3.2%
Stellar age [Gyr]	...	1.0 ± 0.3	NA	NA
Parameter	**Prior[d]**	**Final value[e]**	**Comparison to B21**	**Comparison to H21**
Sampled Transit Parameters				
$\rho_\star$ [g cm^{-3}]	$\mathcal{N}[6.77, 0.63]$	$6.55^{+0.21}_{-0.25}$	↑ 11.5%	↓ 2.3%
Orbital period P_{orb} [days]	$\mathcal{U}[0.668, 0.670]$	$0.66913923^{+0.00000040}_{-0.00000038}$	0%	0%
Transit epoch T_0 [BJD$_{TDB}$ − 2450000]	$\mathcal{U}[2459910.92, 2459910.94]$	$9910.93830^{+0.00037}_{-0.00038}$	N/A[f]	N/A
$R_p/R_\star$	$\mathcal{U}[0.01, 0.04]$	$0.02956^{+0.00057}_{-0.00061}$	↓ 7.2%	↑ 1.6%
b [$R_\star$]	$\mathcal{U}[0, 1]$	$0.266^{+0.062}_{-0.075}$	N/A	N/A
Sampled RV Parameters				
Orbital period P_{orb} [days]	$\mathcal{N}[0.66913923, 0.00000040]$	$0.66913924 \pm 0.00000042$	0%	0%
Transit epoch T_0 [BJD$_{TDB}$ − 2450000]	$\mathcal{N}[9910.93830, 0.00038]$	$9910.93828^{+0.00041}_{-0.00039}$	N/A	N/A
Orbital eccentricity, e	$\mathcal{F}[0]$	0	Locked to 0	Locked to 0
Doppler semiamplitude K [m s^{-1}]	$\mathcal{U}[0, 50]$	$3.76^{+0.39}_{-0.38}$	↓ 17.3%	↓ 11.7%
Derived Planet Parameters				
ΔF [ppm]	...	874^{+34}_{-36}	↓ 14.4%	↓ 14.4%
t_{14} [hr]	...	0.918 ± 0.015	NR	NR
Semimajor axis [au]	...	$0.01138^{+0.00035}_{-0.00034}$	↓ 3.7%	↓ 1.6%
Orbital inclination [deg]	...	$87.17^{+0.81}_{-0.70}$	↑ 2.8%	↑ 1.8%
Planet radius [$R_\oplus$]	...	$1.468^{+0.050}_{-0.051}$	↓ 15.8%	↑ 0.6%
Planet mass [$M_\oplus$]	...	$3.03^{+0.33}_{-0.32}$	↓ 24.8%	↓ 13.2%
Planet density [g cm^{-3}]	...	5.3 ± 0.8	↑ 20.6%	↓ 15.1%
Planet insolation [$S_\oplus$]	...	236 ± 15	↓ 8.1%	NR
Planet equilibrium temperature [K]	...	1062 ± 27	N/A	N/A

Notes. Additional fit results can be found in the Appendix.
[a] An upward arrow in the comparison column indicates that our final value is X% larger than the B21 or H21 value, while a downward arrow indicates that our final value is X% smaller than the B21 or H21 value.
[b] Comparison not possible because the value was not reported in the original publication's summary tables or text.
[c] As reported in H21's Table 1, the L values differ by 11.2%, but see Section 3.1.5 of this work for a discussion on why the offset is likely only 3.7%.
[d] $\mathcal{F}[a]$ refers to a fixed value a, $\mathcal{U}[a, b]$ to a uniform prior between a and b, and $\mathcal{N}[a, b]$ to a Gaussian prior with mean a and standard deviation b.
[e] Inferred parameters and errors are defined as the median and 68.3% credible interval of the posterior distribution.
[f] Comparison not applicable due to a mismatch in units or reporting metric with the original publication's summary tables or text.

dLW). It is thus not surprising that small line asymmetries produced by a relatively inactive star such as TOI-1685 do not produce signals substantial enough to help constrain the GP. Similarly, 2D GPs that incorporate either the Hα or Ca NIR triplet measurements do not provide significant improvements over the simpler 1D model, where we are able to include all three RV instruments' time series. Periodograms of the combined CARMENES and MAROON-X Hα and Ca IR triplet time series do not exhibit singular significant peaks near the rotation period of the star, so their lack of constraining power when added to the GP model is to be expected. Knowing this, we adopt the simpler 1D GP model, which considers the RV time series of all three instruments without any simultaneous stellar variability metrics when determining the lifetime, evolution timescale, period, and amplitude of the GP that is fit alongside the Keplerian planet model.

As both of the discovery papers suggest the potential for an additional planet in the system (at periods of $P = 2.6$ days and $P = 9.025$ days in H21 and B21, respectively), we test five different planetary system models. Each model includes one circular planet initiated at the best-fit period of TOI-1685 b from the joint photometry fit in Section 3.2. The models then have either no additional planet or one additional planet initiated with the orbital parameters presented for the planet candidate in either B21 and H21 that is either restricted to a circular orbit or allowed to be eccentric. We fix the eccentricity of TOI-1685 b to 0, as observational evidence from the Kepler mission shows that small planets with orbital periods shorter

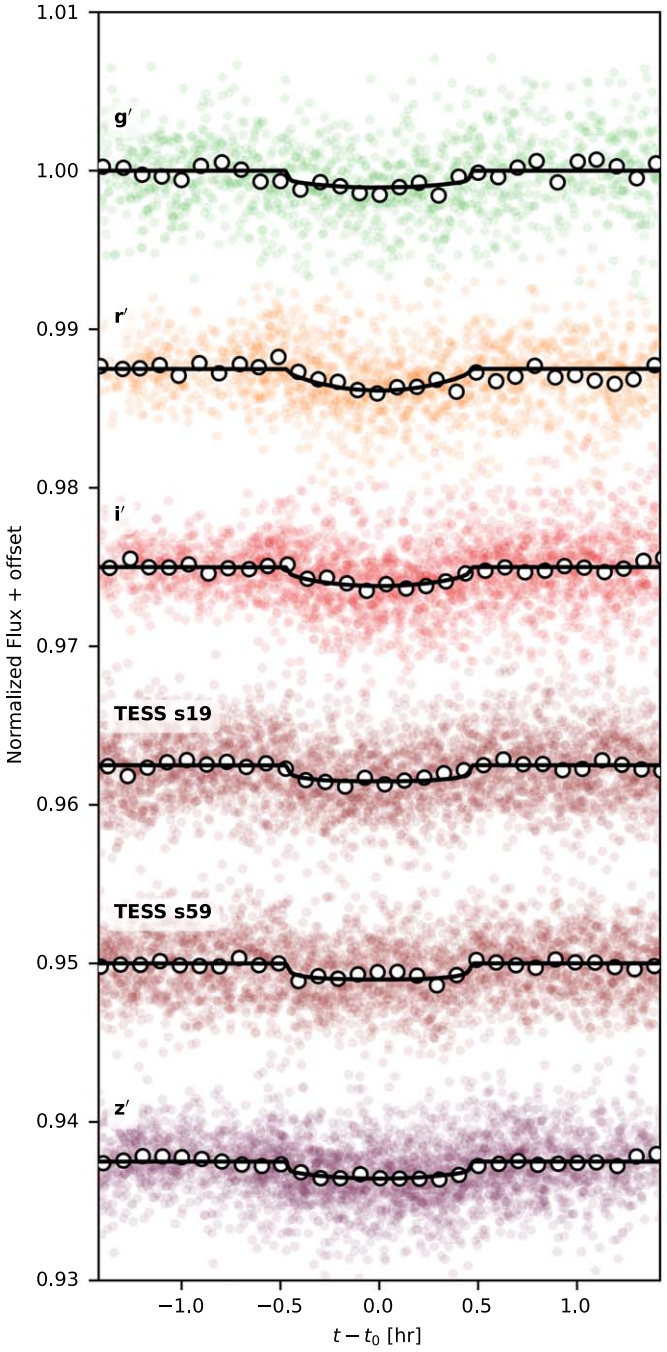

Figure 3. All of the light curves used in the global transit fit of TOI-1685 b, detrended and phase-folded by common photometric bandpass. The two TESS sectors are shown separately. The median transit models are shown with black lines, and the light curves in 6 minute bins are shown as white circles, with error bars generally too small to be visible.

than ∼5 days have eccentricities consistent with 0, as expected due to tidal circularization (see, e.g., Shabram et al. 2016; Van Eylen et al. 2019).

We apply a Gaussian prior on planet b's period and transit epoch taken from the updated TESS + Muscat fits above. For the two planet candidates, we adopt Gaussian priors on the period and epoch taken from their respective announcement publications. Each model also includes a quasiperiodic GP initiated with a uniform prior on the period from 17 to 20 days to address the star's rotational variability. We also implement one floating chunk offset fit, which is a single-planet model that includes only the USP planet without any GP component, as the nightly offsets are expected to remove the effects of any stellar variability occurring on timescales longer than ∼10 hr (see, e.g., Dai et al. 2017).

All six fits produce good agreement in the best-fit period and semiamplitude values for planet b (bottom right panel of Figure 4). To decide which model to adopt, we must first select an appropriate metric for comparing their performance and goodness of fit. We note that the commonly cited Bayesian information criterion is seen to be most useful in selecting the true model for a given system, but this requires the assumption that the true model is included in the set of tested models. Meanwhile, the Akaike information criterion (AIC) is better at selecting the *best* model out of those included in the test set, even if the *true* model is not included. For more on this distinction, see, e.g., Burnham & Anderson (2002) and Chakrabarti & Ghosh (2011). As it is reasonable to assume that we do not have complete knowledge of all planets or stellar variability components for any given exoplanet system, we opt use the AIC as our model comparison metric. When comparing AIC values across the six models described above, we find that the single circular planet model combined with a GP to address the stellar activity is best supported by the data, and so we adopt this as our fiducial RV model.

In our final RV fit, we adopt Gaussian priors on planet b's period and transit epoch from the best-fit transit results in Section 3.2 and lock the planet's eccentricity to 0. We adopt a uniform prior of 17–20 days on the GP period hyperparameter ($P_{\rm GP}$) based on the rotation period reported in B21 and the rotational modulation seen in our combined RV data set and another uniform prior of 1–150 days on the spot lifetime hyperparameter (λ_e), as this corresponds to our 2020 observing baseline, and we do not expect the two observing seasons to be strongly correlated. This produces a best-fit semiamplitude of $K_{\rm b} = 3.76^{+0.39}_{-0.38}$ m s^{-1} (Table 6), which is 11.7% and 17.3% smaller than the best-fit K values from H21 and B21, respectively. The full set of RV fit results is presented in the Appendix in Table A2.

When combined with the updated stellar mass estimate from Section 3.1, $M_\star = 0.454 \pm 0.018\ M_\odot$, and the orbital inclination angle derived from the transit photometry fit, $i = 87.^\circ17^{+0.81}_{-0.70}$, our best-fit RV semiamplitude produces an updated planet mass measurement of $M_{\rm b} = 3.03^{+0.33}_{-0.32}\ M_\oplus$ for TOI-1685 b.

4. Discussion

4.1. Updates to Planet Parameters

Combining the best-fit planet radius from Section 3.2, $R_{\rm b} = 1.468^{+0.050}_{-0.051}\ R_\oplus$, with the best-fit planet mass from Section 3.3, $M_{\rm b} = 3.03^{+0.33}_{-0.32}\ M_\oplus$, produces a best-fit planet density of 5.3 ± 0.8 g cm^{-3}. The similarity to the Earth's bulk density of 5.51 g cm^{-3} suggests that TOI-1685 b is also a rocky planet with minimal volume contributions from any hydrogen or helium atmosphere components (Figure 5).

The RV semiamplitude measured from our combined CARMENES, IRD, and MAROON-X data set is smaller than the values reported in either B21 or H21 (Table 6). While our new value is within 1σ of both previously published results, the 10%–20% decrease in measured RV semiamplitude as more data were added highlights the importance of continued observing, especially in systems with low-mass planets that induce small

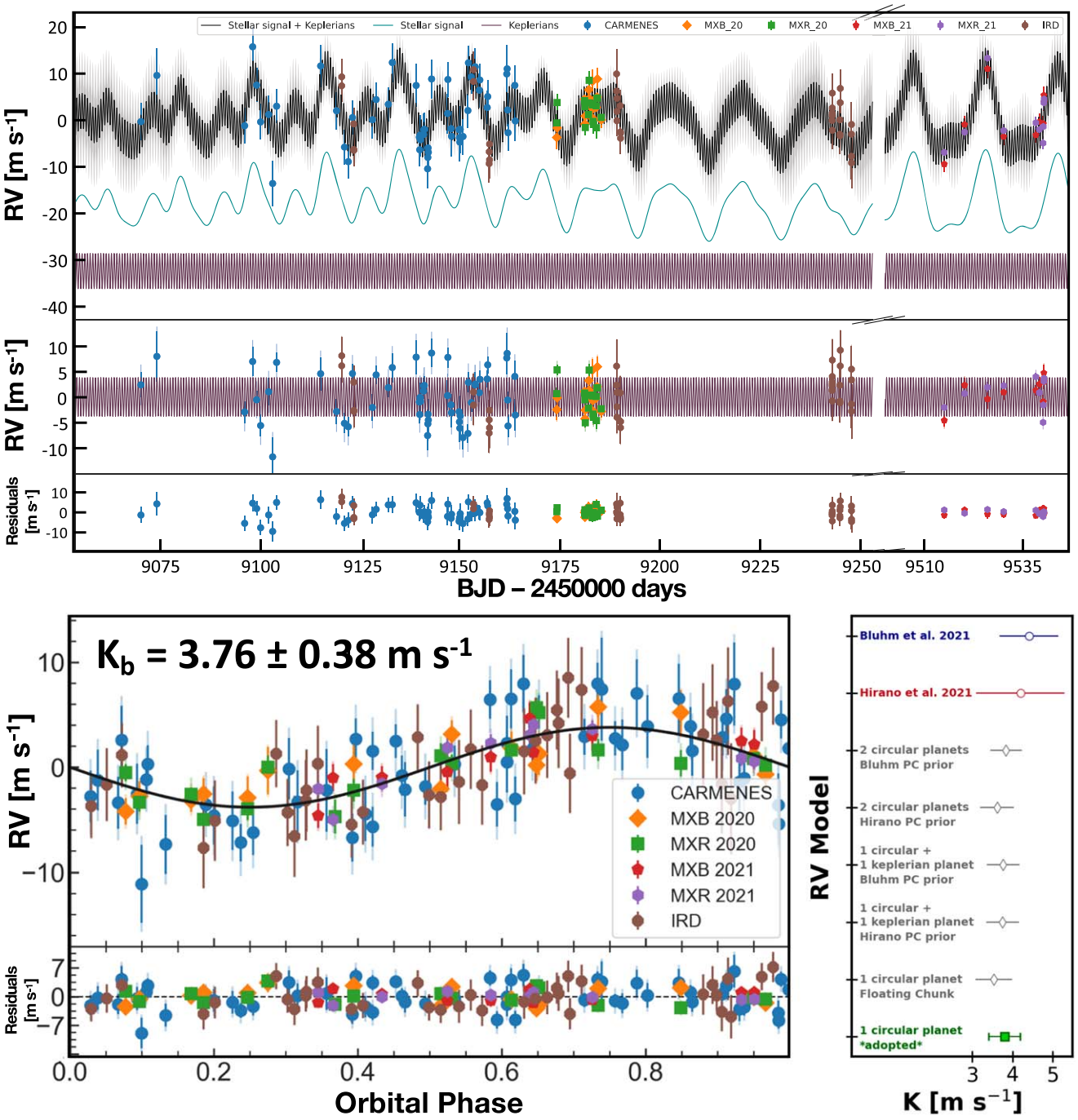

Figure 4. Top: time series RV data used in our adopted one circular planet + 1D quasiperiodic GP fit, color coded by instrument. The MAROON-X data sets are broken up between the 2020 and 2021 semesters due to interventions in the spectrograph that introduce a zero-point offset. The purple line is the model of planet b's orbit, the teal line is the GP representing the star's contribution to the RV signal, and the black line is the planet's orbit combined with the GP. The light shaded areas show the GP model's 1σ and 2σ credible intervals. Bottom left: RV data phase-folded to the best-fit period of planet b. Bottom right: comparison of the best-fit semiamplitudes from the published literature (blue and red points, depicting the results from B21 and H21, respectively) and the different Pyaneti models we tested on the combined IRD + CARMENES + MAROON-X data set. Models with two planets always assume a circular orbit for planet b and then either a circular or Keplerian orbit for the outer planet. We place Gaussian priors on the outer planet candidate's period and transit epoch using the reported planet candidate parameters from B21 and H21. All models produce consistent results for the semiamplitude of planet b, but the preferred solution according to comparisons of the AIC is a single circular planet plus a 1D quasiperiodic GP, which is depicted in green.

RV signals. Planets whose RV semiamplitudes are measured to be slightly too high are more likely to get published than planets whose RV semiamplitudes are measured to be slightly too low when striving to meet 3σ or 5σ detection significance criteria (see, e.g., Burt et al. 2018; Montet 2018), which can in turn bias the small-planet end of the exoplanet mass–radius distribution.

Our measured R_b is in very close agreement with H21 and disagrees with B21 and Laliotis et al. (2023) at the 2.7σ level. This comes in large part from the disagreement in $R_\star$ values derived by B21 (which was also adopted by Laliotis et al. 2023) and H21. The $R_\star$ that we independently derived in Section 3.1.4 is within 0.3σ of the best-fit stellar radius

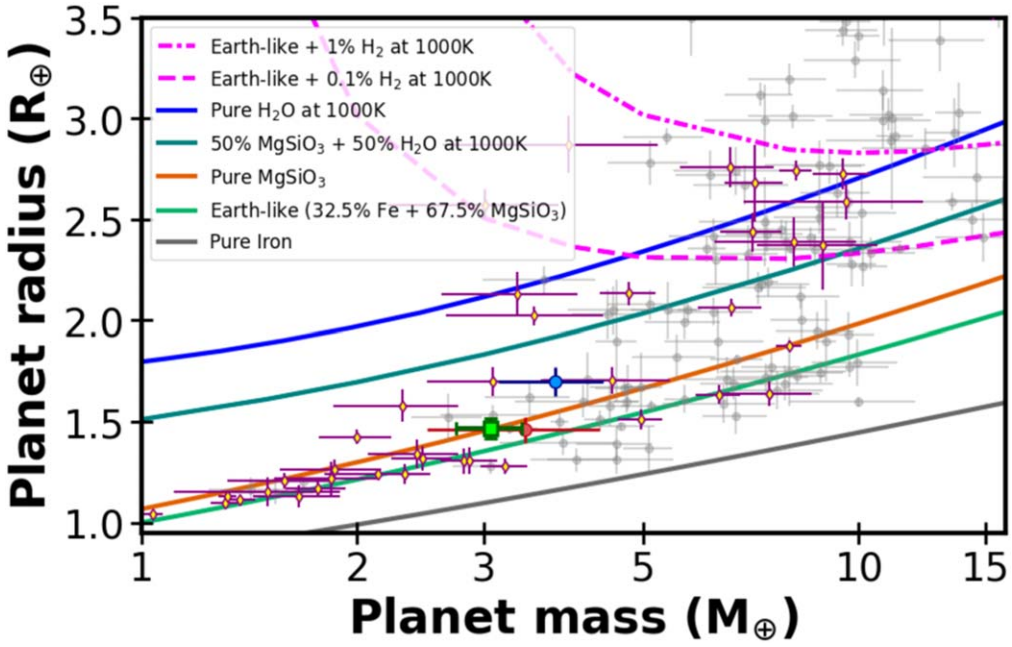

Figure 5. Small planet mass vs radius diagram, using data taken from NASA's Exoplanet Archive on 2023 October 17. Gray points with error bars show confirmed planets with mass and radius measurements better than 20%, and solid lines represent two-layer models as given by Zeng et al. (2016). Large colored circles are the previous characterizations of TOI-1685 b from B21 in blue and H21 in red, while the green square depicts the best-fit mass and radius for the planet derived here. Purple diamonds show planets that have been selected for observation with JWST in Cycle 1 or 2.

from H21, but it is 1.9σ smaller than the $R_\star$ value from B21. Our smaller stellar radius contributes to a smaller planet radius as derived in Section 3.2 and a higher ρ_{pl} when combining the best-fit planet radius and mass. Another contribution to the planet radius disagreements could be the fact that neither of the two nights of MuSCAT2 data that were used in the B21 transit fit passed our screening process (described in Section 2.3) to be included in our joint transit fit, and both of these appear to favor a much larger planet radius.

The updated stellar radius and effective temperature also flow down to impact TOI-1685 b's expected insolation and equilibrium temperature values. The planet's updated stellar insolation, $S = L/a^2$, is $236 \pm 15\ S_\oplus$. Assuming a Bond albedo of $A_B = 0.1$, as suggested by both laboratory astrophysics studies (see, e.g., Essack et al. 2020) and recent JWST observations of the USP super-Earth GJ 367 b (Zhang et al. 2024), TOI-1685 b's equilibrium temperature is 1062 ± 27 K. Given the predominantly $MgSiO_3$ composition suggested by the planet's position on the mass–radius diagram (Figure 5), the internal composition analysis carried out in Section 4.5, and the fact that silicate rocks begin melting at 850 K (Lutgens et al. 2014), TOI-1685 b is likely to be a lava world with a molten dayside surface.

4.2. Interpretation of Previous Planet Candidates

In situ formation for USP planets like TOI-1685 b is deemed unlikely, as their $P < 1$ day orbits lie interior to the dust sublimation radius of typical protoplanetary disks (Millholland & Spalding 2020). Current formation models for these objects generally invoke dynamical interactions with another planet in the system, which drives the USP from a longer period formation location to its current orbital position (see, e.g., Petrovich et al. 2019; Pu & Lai 2019; Millholland & Spalding 2020). An alternative theory puts forth that USPs are the remnant cores of of hot Jupiter or hot Saturn progenitors

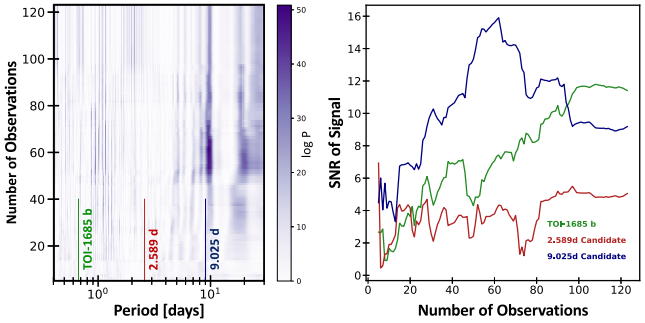

Figure 6. Left: SBGLS periodogram constructed using all of the 2020 RV data for TOI-1685 across the CARMENES, IRD, and MAROON-X instruments. The vertical lines denote the periods of TOI-1685 b (green) and the potential second planets suggested in H21 (red) and B21 (blue). Only TOI-1685 b shows a narrow peak with a roughly monotonic increase in power as a function of the number of observations, the two hallmarks of a Keplerian signal. The H21 signal does not manifest in the combined RVs with any significant power, while the B21 signal exhibits a local maxima in the 50–70 observation range and a broad peak, which suggest it is a signature of activity in the star. Right: detection significance of each period as a function of the number of observations. The signal at TOI-1685 b's period exhibits the roughly monotonic increase expected from a true Keplerian signal, while the signals at the periods corresponding to the H21 and B21 planet candidates show early increases in power followed by a notable downturn or leveling off as more observations are added.

(Jackson et al. 2013, 2016; Valsecchi et al. 2014), but the lack of correlation between USP formation and increased stellar metallicity has resulted in this explanation generally being discarded by the community (Winn et al. 2017). It is therefore reasonable to expect that the TOI-1685 system hosts at least one additional planet that helped to shape the current-day orbit of TOI-1685 b.

However, the two-planet RV models investigated in Section 3.3 using the combined CARMENES, IRD, and MAROON-X data

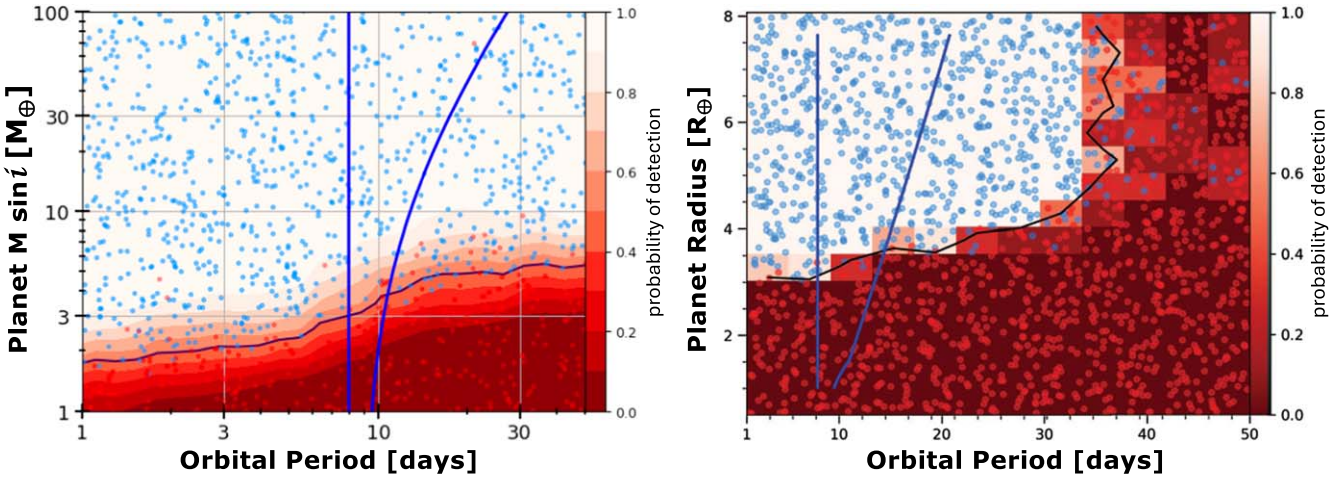

Figure 7. Injection recovery analyses of the residual RVs generated by `Pyaneti` (left) and the combined TESS S19 and S59 light curves (right). Blue and red circles denote synthetic planets that were and were not successfully recovered, respectively. The black contours denote the 50% detection probability threshold as a function of orbital period. In both cases, small and low-mass planets could evade detection, leaving the possibility that TOI-1685 b is not the only low-mass planet in the system. We overplot the allowable parameter space for a perturbing planet if TOI-1685 b started on a 0.05 au orbit as blue lines, using the mass–radius relation from Müller et al. (2024) to convert the planet masses from Figure 8. For the perturber to remain undetected, it would need to have a mass $\leqslant 3\ M_{\oplus}$ and a radius $\leqslant 3\ R_{\oplus}$ if on the shorter (8 days) end of the allowable period range. The undetected planet limits relax to $\leqslant 5\ M_{\oplus}$ and $\leqslant 3.75\ R_{\oplus}$ when considering a perturber on the longer (27 days) end of the allowed orbital period range.

sets do not support the inclusion of additional planets in the best-fit RV model for this system. To confirm that our GP model is not absorbing additional signals induced by these two-planet candidates, we carry out a set of tests that inject two synthetic planets into the stellar activity time series model produced by Pyaneti (teal line in the top panel of Figure 4). In one instance, we inject a synthetic planet b, using the best-fit orbital parameters from our fit, alongside a synthetic planet matching the candidate suggested in H21. In the second instance, we insert the same synthetic planet b and a synthetic planet c matching the candidate put forth in B21. We replicate our true data sets by selecting the model RV points closest in time to the actual observations and adopting the corresponding RV errors. We then fit each data set with both a one- and a two-planet model, using the same priors for planet b and the GP as applied in our final RV model. We include uniform priors for the second planet using the 1σ uncertainties from the H21 and B21 results. In both cases, comparison of the AIC values from the one- and two-planet models shows a clear preference for the two-planet model: $\Delta\mathrm{AIC} = 44$ in the H21 candidate case and 13 in the B21 candidate case. Thus, we can be confident that if there was a second planet in the data with orbital parameters matching either of the previously published candidates, the AIC comparison would point to the two-planet fit as the preferred model. As this is not the case, we rule out the Keplerian nature of the planet candidates suggested in the original B21 and H21 discovery papers.

To investigate these signals further, we generate a stacked Bayesian generalized Lomb–Scargle (SBGLS) periodogram using the SBGLS code[21] presented in Mortier & Collier Cameron (2017). This approach begins by calculating a Bayesian generalized Lomb–Scargle (BGLS) for the first N points of an RV time series—we adopt $N = 10$—and then iteratively adds the next RV measurement in the series and recalculates the BGLS periodogram until the entire RV time series has been included. At this point, all of the BGLS periodograms are normalized with their respective minimum values so that one can compare how the strength of a given periodic signal grows or fades with the number of observations included.

We only include observations taken during the 2020 observing campaigns in order to better replicate the timescale and stellar surface conditions present in the CARMENES and IRD data sets. True Keplerian signals are expected to increase their significance roughly monotonically as more data points are added and should present as narrow features over timescales that are notably longer than the planet's period thanks to their exact period repetition orbit after orbit (e.g., Hatzes 2013; Suárez Mascareño et al. 2017; Burt et al. 2021; Laliotis et al. 2023). TOI-1685 b's signal in the stacked periodogram meets both of these criteria, further corroborating its planetary nature (Figure 6).

The stacked periodogram does not show significant power at the 2.6 day period suggested for the planet candidate in H21, despite the higher RV precision provided by the CARMENES and MAROON-X data. H21 estimated the semiamplitude of the signal to be $\sim 6\ \mathrm{m\ s^{-1}}$, corresponding to a planet mass of 7–8 $M_{\oplus}$. Using the publicly available `RVSearch` package (Rosenthal et al. 2021), we carry out an injection/recovery analysis of the combined RV data set and find that the existing data should be sensitive to planets down to $\sim 1\ M_{\oplus}$ at this 2.6 day period (Figure 7). Given the lack of signal in our longer-baseline and higher-precision data set, we assert that the 2.6 day H21 signal is due to a nonplanetary source. The true origin of the signal is not immediately obvious. It could be driven by instrumental systematics, aliases within the IRD data, or even short-term variability in the star. Regardless, additional targeted investigation would be required to identify its origin.

The 9 day period of the planet candidate suggested in B21 does show significant power in the stacked periodogram, especially in the $N = 50$–70 observation range. But the power decreases as additional observations are added to the combined RV data set, making that peak a local maximum rather than a sustained detection. This characteristic of showing a probability maximum and then decreasing as additional data are added is used to rule out the Keplerian nature of a similar 19 day signal detected in the CARMENES RVs in B21 and to attribute that

[21] https://anneliesmortier.wordpress.com/sbgls/

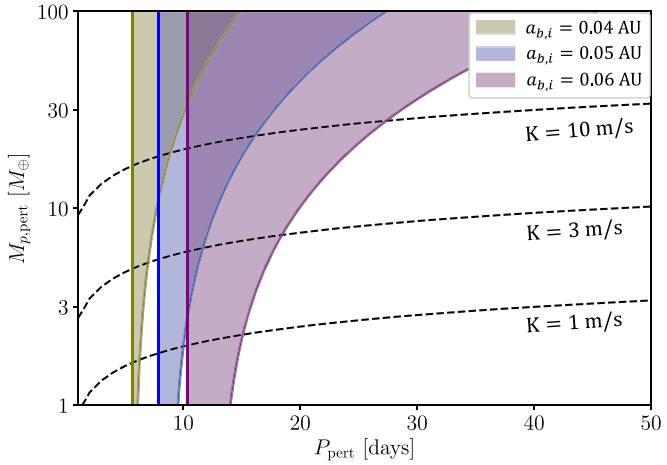

Figure 8. Period and mass of a hypothetical perturber that could have caused TOI-1685 b to decay to its current orbit via obliquity tides. The shadings indicate different possible *initial* semimajor axes of TOI-1685 b before its decay. Each region is bounded on the left by a minimum initial period ratio, $P_{\mathrm{pert}}/P_{b,i} = 1.3$, and on the right by $|g|/\alpha = 1$ (with $|g|/\alpha$ increasing to the left). The dashed black lines indicate contours of constant RV semiamplitude.

peak in the periodogram to stellar variability. Given the lack of sustained power increase and the relatively wide peak that the 9 day signal exhibits in the stacked periodogram (which can be suggestive of differential rotation, rather than a planet on a well-defined orbit; see, e.g., Mortier & Collier Cameron 2017), we now ascribe the 9 day signal to stellar variability as well. Significant signals at the harmonics of the star's rotation (P/2, P/3, etc.) are common in RV periodograms (see, e.g., Boisse et al. 2011), though this is not explicitly required, and activity signals can emerge at non-rotation-related periods as well (Nava et al. 2020).

4.3. Remaining Possibilities for a Companion Planet

While these two signals do not appear to be bona fide planets that could have shepherded TOI-1685 b onto its USP orbit, there is still a range of dynamical parameter space in the system that could hold additional planets. Using the `RVSearch` python package (Rosenthal et al. 2021), we inject a population of synthetic planets into the residual RVs from Pyaneti and test what combinations of planet mass and orbital period should be detectable in the RV data sets presented in this work (Figure 7). We perform a similar transit injection recovery analysis using the combined Sector 19 and Sector 59 light curves from the TESS SPOC 2 minute observations for TOI-1685. The transit signal of the known planet is masked out using its best-fit ephemeris to obtain the residual light curve. The injected planets are drawn from a log-uniform grid in period (1–50 days) and radius (0.5–8 $R_\oplus$), with randomized ephemeris and impact parameters. We use the box least-squares (BLS) algorithm to search for the injected signal. The signal is considered "recovered" if the ratio of its BLS signal to the pink noise passes a threshold value of 9 and the recovered signal has a period within at least 2σ of the injected period using the ephemeris-matching algorithms from Coughlin et al. (2014).

As one summary metric, we calculate the planet mass that corresponds to a 50% detection probability on a 50 day orbit, equivalent to a semimajor axis of 0.20 au, as Sanchis-Ojeda et al. (2014) showed that most USP super-Earth planets have companions with periods $P < 50$ days. With the existing RV data, `RVSearch` shows that planets with $M_{pl} \leqslant 8\ M_\oplus$ on 50 day orbits could go undetected. The TESS data, limited to just 56 total days of observation, are sensitive to planets down to $\sim 3\ R_\oplus$ on periods shorter than 10 days, but planets up to $8\ R_\oplus$ would likely go undetected in a BLS search if their periods exceed 40 days. Both results thus leave open the possibility that TOI-1685 b could have a nearby, low-mass planet companion.

4.4. Investigations into a Perturbing Companion Planet

Given these detection limits, it is worthwhile to determine the parameters of a hypothetical perturbing planet that could have driven TOI-1685 b's migration to its current orbit. We consider obliquity-driven tidal migration (Millholland & Spalding 2020) for this exercise, noting that other pathways are also possible. In order for the mechanism to operate, the system needed to begin with $|g|/\alpha > 1$, where $g = \dot{\Omega}$ is the nodal precession rate of TOI-1685 b triggered by its companion and α is its spin-axis precession rate. We use our derived system parameters and also assume TOI-1685 b's Love number to be $k_2 = 0.2$ and moment-of-inertia factor to be $C = 0.3$, although the results are not strongly sensitive to these choices. In Figure 8, we plot the constraints on the period and mass of the hypothetical perturbing planet. The constraints depend on the unknown starting location of TOI-1685 b, so we consider three possible initial semimajor axes, $a_{b,i}$, at 0.04, 0.05, and 0.06 au. We select this range (which corresponds to the semimajor axis range inhabited by the innermost planets in compact multiplanet systems) because several USP formation theories, including the obliquity tides theory used here, posit that USPs started out at the inner edge of a compact multiplanet system and migrated inward. The shaded regions indicate where the initial $|g|/\alpha > 1$ for the chosen $a_{b,i}$, and they are bounded on the right by $|g|/\alpha = 1$ and on the left by a minimum initial period ratio, $P_{\mathrm{pert}}/P_{b,i} = 1.3$. We also plot contours of the RV semiamplitude of the hypothetical perturber.

Taking the middle option, where TOI-1685 b formed in a 0.05 au ($P \sim 6$ days) orbit, the perturber must have an orbital period between 7.9 and 27.4 days and a mass between 1 and 100 $M_\oplus$, with increased mass necessary at longer periods. We outline this parameter space on the RV and transit injection/recovery grids presented in Figure 7 and note that for the perturber to remain undetected, it would need to have a mass $\leqslant 3\ M_\oplus$ and a radius $\leqslant 3\ R_\oplus$ if on the shorter (8 days) end of the allowable period range. The undetected planet limits relax to $\leqslant 5\ M_\oplus$ and $\leqslant 3.75\ R_\oplus$ when considering a perturber on the longer (27 days) end of the allowed orbital period range.

4.5. Interior Models

Given the small radius, Earth-like density, and hot equilibrium temperature of the planet, we do not expect it to have retained any significant H/He atmosphere that may have accumulated during planet formation (Rogers 2015; Lopez 2017). The presence of a significant water layer on the planet is also unlikely, given how closely the planet falls to the Earth-like and pure $MgSiO_3$ model lines on the mass–radius diagram (Figure 5) and how well its density aligns with the rocky-worlds population of the trimodal distribution of small planets around M dwarfs that distinguishes rocky planets from water- and gas-rich worlds (Luque & Pallé 2022).

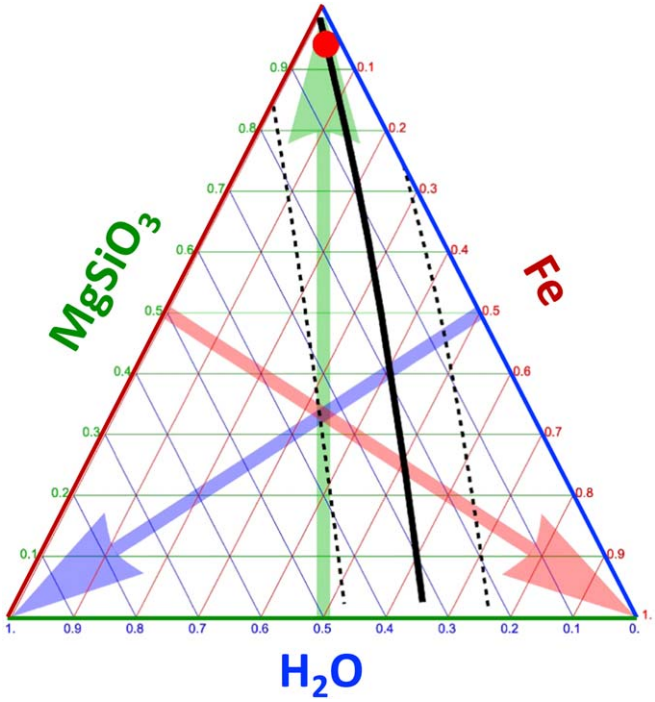

Figure 9. Ternary plot depicting different fractional combinations of water, rock, and iron for solid planet compositions. The solid and dashed black lines mark the possible position of TOI-1685 b and the 68% credible intervals. The red dot depicts the model planet at an estimated internal pressure of $P_0 = 600$ GPa, which results in relative mass fractions of 94.2% $MgSiO_3$, 3.3% Fe, and 2.5% H_2O.

We use the `Manipulate Planet` tool[22] to estimate the interior composition of TOI-1685 b using a three-layer model comprised of iron, water, and magnesium silicate. To estimate the planet's central pressure, P_o, we scale the Earth's central pressure of 600 Gpa by M_{pl}^2/R_{pl}^4, producing an estimate of $P_o \approx 600$ GPa. This central pressure, combined with our best-fit measurements of the planet's mass and radius, produces an interior model dominated by magnesium silicate (Figure 9). Specifically, the three-component mass fractions are 94.2% $MgSiO_3$, 3.3% Fe, and 2.5% H_2O, and the corresponding radius components are $R_{MgSiO_3} = 1.08\ R_\oplus$, $R_{Fe} = 0.34\ R_\oplus$, and $R_{H_2O} = 0.046\ R_\oplus$.

4.6. Implications for Atmospheric Characterization

The updated stellar and planet parameters derived in this work impact the planet's estimated potential for atmospheric characterization. The standard metrics for assessing this potential are the transmission and emission spectroscopy metrics (TSM and ESM), defined in Equations (1) and (4) of Kempton et al. (2018). The TSM is proportional to the transmission spectroscopy signal of a planet based on the expected strength of its spectral features and the *J*-band magnitude of the host star, while the ESM is proportional to the secondary eclipse signal at mid-IR wavelengths based on the planet's size and temperature and the *K*-band magnitude of the host star. At present, TOI-1685 b will be targeted by three separate JWST programs: two transmission spectroscopy programs using the NIRSPEC/BOTS (Jakobsen et al. 2022) and NIRISS/SOSS (Doyon et al. 2012) configurations and one thermal emission program using NIRSPEC/BOTS.

Inserting our new planet and stellar parameters results in an updated TSM value of 12.4 ± 2.0, which just barely surpasses the TSM = 12 cutoff suggested for identifying the best JWST targets smaller than 1.5 $R_\oplus$ (Kempton et al. 2018). However, for the accepted NIRSPEC observations (Fisher et al. 2023; Luque et al. 2023), the fact that TOI-1685 is an M dwarf and therefore brighter in the *K* band than in the *J* band ($J - K_s = 0.858$ mag) bodes well, as the G395 band of NIRSpec starts at 2.8μm and the *K* band's central wavelength of $\sim$2.2μm better approximates the star's G395 brightness than the *J* band's 1.25μm center.

Updating the ESM value of TOI-1685 b using our new planet and stellar parameters gives $ESM = 11.9 \pm 1.3$. This exceeds the cutoff value of 7.5 suggested for identifying the top emission spectroscopy small planets for JWST in Kempton et al. (2018) and is a promising starting point for the thermal emission observations.

In order to accurately constrain the atmospheric properties of any exoplanet, one requires a certain precision on the mass and radius. Several studies have attempted to quantify the precision requirement on the planet mass; in particular, Batalha et al. (2019) concluded that a $\pm$50% mass precision is sufficient for initial characterization with JWST, while $\pm$20% is required for more detailed analyses. At the $\pm$20% level, the width of the posterior distributions, from an atmospheric retrieval analysis, for example, are dominated by the observational uncertainties. In contrast, Di Maio et al. (2023) determined that a mass precision of just $\pm$50% was sufficient to obtain reliable retrieval results, even in the case of a high mean molecular weight atmosphere. However, this study was done in the context of Ariel spectra and relies on the assumption that one can accurately retrieve the planet mass from a spectroscopic analysis, which may be challenging due to degeneracies between mass and composition (Batalha et al. 2017). Our new constraints on the mass of TOI-1685 b provide a precision of $\sim\pm$10%, which will enable a detailed characterization of any potential atmosphere on this planet.

Furthermore, the scale height of the atmosphere, which has a significant effect on the size of all the spectral features, is given by

$$H = \frac{k_B T}{\mu g}, \tag{2}$$

where T is the atmospheric temperature, μ is the mean molecular weight, g is the surface gravity, and k_B is the Boltzmann constant. This leads to a direct degeneracy between the surface gravity, determined through the planetary mass and radius, and the mean molecular weight of the atmosphere. A key science goal of JWST is to establish the presence and nature of the atmospheres of smaller planets, which are unlikely to be hydrogen-dominated. In the case of TOI-1685 b, future JWST observations hope to observe its possible atmosphere, and measuring the mean molecular weight will provide some constraints on its chemical composition. Our updated mass and radius give a value for the surface gravity of 1378^{+262}_{-226} cm s^{-2}, a precision of <20%. This should enable one to determine μ

[22] https://www.cfa.harvard.edu/~lzeng/manipulateplanet.html

from the transmission spectra and distinguish between different atmospheric scenarios.

5. Conclusion

Here we present an updated analysis of the small, ultrashort-period planet orbiting the nearby M dwarf star TOI-1685. This planet was first identified by NASA's TESS mission, and the host star was then followed up photometrically from the ground by the MuSCAT telescope network, the Mont-Mégantic Observatory (OMM) telescope's PESTO camera, and LCO's Sinistro camera, which provided additional transit photometry used to refine the planet's radius. The star has also been observed by the CARMENES, IRD, and MAROON-X spectrographs, which provide precise RV measurements that are used to determine the planet's mass.

We highlight the importance of the stellar characterization phase of any exoplanet confirmation effort, as study of the star's photometric metallicity reveals that it lies 0.57 mag above the main sequence and must therefore be metal-rich ($[\mathrm{Fe/H}] = +0.3 \pm 0.1$). This increased stellar metallicity affects the star's mass and radius estimates as derived using the absolute magnitude–metallicity–mass and absolute magnitude–metallicity–radius calibrations from Mann et al. (2015) and Mann et al. (2019), respectively. . This in turn impacts the planet's derived mass and radius values, as these are indirect measurements and report the planet's mass and radius relative to its host star. Our updated stellar and planetary mass and radius values are as follows: $R_\star = 0.4555 \pm 0.0128\ R_\odot$, $M_\star = 0.454 \pm 0.018\ M_\odot$, $R_\mathrm{p} = 1.468^{+0.050}_{-0.051}\ R_\oplus$, and $M_\mathrm{p} = 3.03^{+0.33}_{-0.32}\ M_\oplus$. Together, the planetary mass and radius produce a best-fit bulk density value of $\rho_\mathrm{p} = 5.3 \pm 0.8$ g cm^{-3}, just 4% less than the Earth's bulk density of 5.51 g cm^{-3}. Combining our updated luminosity ($L_\star = 0.03052 \pm 0.00061\ L_\odot$) and effective temperature ($T_\mathrm{eff} = 3575 \pm 53$ K) estimates for the star with the planet's orbital period and assumed Bond albedo of 0.1 produces an estimated equilibrium temperature of $T_\mathrm{eq} = 1062 \pm 27$ K for TOI-1685 b.

Our updated transit and RV analyses suggest that TOI-1685 falls between the planet solutions presented in the B21 and H21 discovery papers (Figure 5). The planet is smaller and less massive than suggested in B21 (with the radius decreasing by 15.8% and the mass decreasing by 24.8%) and roughly the same size but less massive than the best-fit results from H21 (with the radius increasing by 0.6% and the mass decreasing by 13.2%). Follow-up efforts to confirm and obtain masses for transiting planets are often required to pass a mass precision threshold before being considered ready for publication (3σ and 5σ being common break points). There is thus a possibility that planets whose RV semiamplitudes are measured to be slightly too high are more likely to get published than planets whose RV semiamplitudes are measured to be slightly too low. This can influence which planets appear in the literature and are therefore included on the low-mass end of exoplanet mass–radius diagrams and may then bias our mass–radius relations (see, e.g., Burt et al. 2018; Montet 2018). While time-intensive, it is nonetheless important to continue RV monitoring of small planets past their initial publication to minimize such biases.

We do not find sufficient evidence to confirm the planetary nature of the additional planet candidates put forth in the H21 and B21 publications. The 9 day signal in B21 appears prominently in the combined RV data set but is likely a $P_\mathrm{rot}/2$ manifestation of the star's rotational modulation based upon an SBGLS analysis. The 2.6 day signal suggested in H21 does not present at a significant level in the combined RV data set, despite the increased observational baseline and RV precision, and so we assume it is a systematic tied to the original IRD data. A set of injection/recovery analyses applied to the RV and TESS data, however, reveal that small ($R_{pl} < 3.75\ R_\oplus$) and low-mass ($M_{pl} < 5\ M_\oplus$) planets could still remain hidden in the existing data on orbits of less than 30 days.

When investigating the parameters of a hypothetical second perturbing planet that could have driven TOI-1685 b's migration to its current orbit via obliquity tides, we find that if TOI-1685 b formed at a separation of 0.05 au ($P \sim 6$ days), then the perturber must have an orbital period between 7.9 and 27.4 days and a mass from 1 to 100 $M_\oplus$ with increased mass necessary at longer periods. For such a planet to remain undetected, it would need to have a mass $\leqslant 3\ M_\oplus$ and a radius $\leqslant 3\ R_\oplus$ if on the shortest end of that period range. The planet could, however, be as massive as 5 $M_\oplus$ and as large as 3.75 $R_\oplus$ and still avoid detection in the existing RV and photometry data if on the longest end of the allowed period range.

Obtaining planet masses and radii that are both precise *and* accurate is especially crucial in the era of TESS and JWST. As noted in the beginning of this Letter, TOI-1685 b is the subject of three accepted JWST proposals scheduled for observation in Cycle 2, two of which focus on the planet's status as a bona fide water world, while the third aims to measure its oxidation as a hot rocky super-Earth. Our new mass and radius measurements deem the water-world scenario unlikely, but a high mean molecular weight atmosphere is still plausible, though more challenging to observe. Even in the absence of any atmosphere, however, the phase curve measurements could still provide information about the planet's interior composition. In any case, our improved mass and radius constraints will be essential for correctly interpreting these upcoming observations.

The TESS mission continues to produce thousands of tantalizing small exoplanet candidates, far more than can be thoroughly confirmed and characterized by the limited number of oversubscribed high-precision RV spectrographs currently in operation. Ensuring that the TOIs most likely to be included in the *even more* oversubscribed JWST schedule have undergone sufficient follow-up and characterization (both of the planets and of their host stars) to know that they are truly appropriate targets for the stated JWST science goals should be a primary focus of the exoplanet community moving forward.

Acknowledgments

Part of this research was carried out at the Jet Propulsion Laboratory, California Institute of Technology, under a contract with the National Aeronautics and Space Administration (NASA). E.G. was supported by NASA NSF Astronomy & Astrophysics Research Program grant 1817215, NASA Exoplanets Research Program grant 80NSSC20K0251, and NASA TESS Guest Observer Cycle 4 Award 80NSSC22K0295. The University of Chicago group acknowledges funding for the MAROON-X project from the David and Lucile Packard Foundation, the Heising-Simons Foundation, the Gordon and Betty Moore Foundation, the Gemini Observatory, the NSF (award No. 2108465), and NASA (grant No. 80NSSC22K0117).

We follow the guidelines of NASA's Transform to OPen Science (TOPS) mission for our open science practices (NASA

TOPS Open Science 101 Curriculum Development Team et al. 2023).

This Letter includes data collected by the TESS mission. Funding for the TESS mission is provided by the NASA Explorer Program. Resources supporting this work were provided by the NASA High-End Computing (HEC) Program through the NASA Advanced Supercomputing (NAS) Division at Ames Research Center for the production of the SPOC data products.

The TESS data presented in this Letter were obtained from the Mikulski Archive for Space Telescopes (MAST) at the Space Telescope Science Institute and can be accessed via doi:10.17909/h9bv-4e03. Support for MAST for non-HST data is provided by the NASA Office of Space Science via grant NNX13AC07G and by other grants and contracts.

This work was enabled by observations made from the Gemini North telescope, located within the Maunakea Science Reserve and adjacent to the summit of Maunakea. We are grateful for the privilege of observing the Universe from a place that is unique in both its astronomical quality and its cultural significance. The Gemini observations presented in this work are associated with programs GN-2020B-Q-234 and GN-2021B-Q-230.

The software used to execute most analyses in this Letter and to generate the corresponding figures is hosted on GitHub.[23]

This research has made use of the NASA Exoplanet Archive, which is operated by the California Institute of Technology, under contract with the National Aeronautics and Space Administration under the Exoplanet Exploration Program. This research has also made use of the Exoplanet Follow-up Observation Program website, which is operated by the California Institute of Technology, under contract with the National Aeronautics and Space Administration under the Exoplanet Exploration Program.

This research has made use of NASA's Astrophysics Data System Bibliographic Services.

This research made use of Astropy, a community-developed core Python package for Astronomy (Astropy Collaboration et al. 2013, 2018, 2022).

Based on observations obtained with PESTO at the Mont-Mégantic Observatory, funded by the Université de Montréal, Université Laval, the Natural Sciences and Engineering Research Council of Canada (NSERC), the Fond québécois de la recherche sur la Nature et les technologies (FQRNT), and the Canada Economic Development program.

We thank Li Zeng for guidance on the ManipulatePlanet tool. We thank Akihiko Fukui, John Livingston, and the MuSCAT team for sharing the MuSCAT light curves originally presented in Hirano et al. (2020) for use in this work. We also thank Hannu Parviainen and the MuSCAT2 team for sharing a custom reduction of all of the available MuSCAT2 observations of TOI-1685 and advice on their use.

We also thank the anonymous referee for the time and care in reviewing this Letter. The suggestions improved the clarity, depth, and utility of this work.

Facilities: TESS, OAO:1.88m, Sanchez, FTN, LCOGT OMM:1.6, Gemini:Gillett Subaru, CAO:3.5m

Software: `ARIADNE` (Vines & Jenkins 2022), `Astropy` (Astropy Collaboration et al. 2022), `BANYAN Σ` (Gagné et al. 2018), `batman` (Kreidberg 2015), `celerite` (Foreman-Mackey et al. 2017), `dynesty` (Speagle 2020), `juliet` (Espinoza et al. 2019), `Manipulate Planet` (Zeng et al. 2016), `Pyaneti` (Barragán et al. 2019, 2022), `RVSearch` (Rosenthal et al. 2021), `SBGLS` (Mortier & Collier Cameron 2017), `SERVAL` (Zechmeister et al. 2018), `VOSA` (Bayo et al. 2008).

Appendix
Transit Model Limb Darkening, GP, Baseline, and Noise Parameters

The full set of best-fit parameters for the Transit Light Curve Model described in Section 3.2 are presented in Table A1. Both the model priors and best-fit parameters for the Radial Velocity Model described in Section 3.3 are presented in Table A2.

Table A1
Best-fitting Values for the Limb Darkening, GP, Baseline, and Noise Parameters in the Transit Model Described in Section 3.2

Parameter [Unit]	Value	Parameter [Unit]	Value	Parameter [Unit]	Value
$q_{1,\mathrm{TESS}}$	$0.48^{+0.2}_{-0.19}$	δy_{M12z}	-0.0007 ± 0.00022	$\mathrm{am}_{\mathrm{M22z}}$	0.0 ± 0.00019
$q_{2,\mathrm{TESS}}$	$0.161^{+0.11}_{-0.097}$	$\mathrm{FWHM}_{\mathrm{M12z}}$	$-0.00006^{+0.00022}_{-0.00023}$	δx_{M22z}	$-0.00001^{+0.0003}_{-0.00029}$
$q_{1,g'}$	$0.25^{+0.16}_{-0.14}$	$\mathrm{peak}_{\mathrm{M12z}}$	-0.0001 ± 0.00019	δy_{M22z}	-0.0 ± 0.00027
$q_{2,g'}$	$0.74^{+0.16}_{-0.2}$	c_{M13g}	$-0.00305^{+0.00031}_{-0.0003}$	$\mathrm{FWHM}_{\mathrm{M22z}}$	0.00008 ± 0.00029
$q_{1,r'}$	$0.83^{+0.11}_{-0.12}$	$\sigma_{\mathrm{w,M13g}}$ [ppm]	24^{+110}_{-20}	c_{M31g}	$-0.00012^{+0.00024}_{-0.00025}$
$q_{2,r'}$	$0.82^{+0.1}_{-0.12}$	$\mathrm{am}_{\mathrm{M13g}}$	$0.00446^{+0.00047}_{-0.00048}$	$\sigma_{\mathrm{w,M31g}}$ [ppm]	46^{+120}_{-35}
$q_{1,i'}$	$0.57^{+0.15}_{-0.14}$	δx_{M13g}	$-0.00008^{+0.00043}_{-0.00042}$	$\mathrm{am}_{\mathrm{M31g}}$	$0.00101^{+0.0002}_{-0.00019}$
$q_{2,i'}$	$0.7^{+0.17}_{-0.2}$	δy_{M13g}	$0.00112^{+0.00037}_{-0.00036}$	δx_{M31g}	$0.00028^{+0.00032}_{-0.00033}$
q_{1,z_s}	$0.27^{+0.15}_{-0.13}$	$\mathrm{FWHM}_{\mathrm{M13g}}$	$-0.00089^{+0.00059}_{-0.00058}$	δy_{M31g}	0.00011 ± 0.00023
q_{2,z_s}	$0.75^{+0.16}_{-0.2}$	$\mathrm{peak}_{\mathrm{M13g}}$	-0.00178 ± 0.0008	$\mathrm{FWHM}_{\mathrm{M31g}}$	-0.00021 ± 0.00046
$\mathrm{GP}_{\mathrm{S0,1}}/10^{10}$	$9.3^{+23.0}_{-5.8}$	c_{M13z}	0.0002 ± 0.00022	$\mathrm{peak}_{\mathrm{M31g}}$	$-0.00122^{+0.00039}_{-0.0004}$
$\mathrm{GP}_{\mathrm{P,1}}$ [days]	$4.9^{+6.7}_{-3.7}$	$\sigma_{\mathrm{w,M13z}}$ [ppm]	250^{+170}_{-200}	c_{M31r}	$-0.00073^{+0.00025}_{-0.00024}$
$\mathrm{GP}_{\mathrm{S0,2}}/10^{10}$	34^{+22}_{-12}	$\mathrm{am}_{\mathrm{M13z}}$	$-0.00078^{+0.00019}_{-0.0002}$	$\sigma_{\mathrm{w,M31r}}$ [ppm]	160^{+190}_{-100}
$\mathrm{GP}_{\mathrm{P,2}}$ [days]	$3.3^{+1.2}_{-1.0}$	δx_{M13z}	-0.00012 ± 0.00014	$\mathrm{am}_{\mathrm{M31r}}$	0.00007 ± 0.00011
c_{TESS19}	$-0.000071^{+0.000032}_{-0.000031}$	δy_{M13z}	-0.00019 ± 0.00016	δx_{M31r}	$0.00009^{+0.00022}_{-0.00023}$
$\sigma_{\mathrm{w,TESS19}}$ [ppm]	16^{+26}_{-11}	$\mathrm{FWHM}_{\mathrm{M13z}}$	0.00079 ± 0.00025	δy_{M31r}	0.00019 ± 0.00018
c_{TESS59}	$-0.000071^{+0.000047}_{-0.000049}$	$\mathrm{peak}_{\mathrm{M13z}}$	$0.00007^{+0.00023}_{-0.00022}$	$\mathrm{FWHM}_{\mathrm{M31r}}$	$0.00045^{+0.0003}_{-0.00029}$

[23] https://github.com/JenniferBurt/TOI-1685b

Table A1
(Continued)

Parameter [Unit]	Value	Parameter [Unit]	Value	Parameter [Unit]	Value
$\sigma_{w,TESS9}$ [ppm]	34^{+75}_{-26}	c_{M21r}	$-0.0005^{+0.00054}_{-0.00053}$	$peak_{M31r}$	0.00065 ± 0.00026
c_{M11z}	0.00019 ± 0.00024	$\sigma_{w,M21r}$ [ppm]	9944^{+39}_{-65}	c_{M31i}	$-0.00061^{+0.00023}_{-0.00022}$
$\sigma_{w,M11z}$ [ppm]	$11.2^{+110.0}_{-9.0}$	am_{M21r}	$0.00105^{+0.00077}_{-0.00076}$	$\sigma_{w,M31i}$ [ppm]	$5.9^{+20.0}_{-4.1}$
am_{M11z}	$-0.000594^{+0.000096}_{-0.000098}$	δx_{M21r}	0.002 ± 0.0013	am_{M31i}	-0.000284 ± 0.000084
δx_{M11z}	0.00052 ± 0.00017	δy_{M21r}	$0.0015^{+0.00068}_{-0.0007}$	δx_{M31i}	0.00013 ± 0.00014
δy_{M11z}	-0.00001 ± 0.0002	$FWHM_{M21r}$	-0.0001 ± 0.0013	δy_{M31i}	-0.00017 ± 0.00015
$FWHM_{M11z}$	-0.00078 ± 0.00033	c_{M21i}	$-0.00035^{+0.00031}_{-0.0003}$	$FWHM_{M31i}$	$0.00071^{+0.00025}_{-0.00026}$
$peak_{M11z}$	-0.00135 ± 0.00029	$\sigma_{w,M21i}$ [ppm]	5690^{+170}_{-160}	$peak_{M31i}$	0.00101 ± 0.00023
c_{M12g}	$-0.00477^{+0.00029}_{-0.00028}$	am_{M21i}	$0.00073^{+0.00048}_{-0.00051}$	c_{M31z}	$0.0^{+0.00022}_{-0.00023}$
$\sigma_{w,M12g}$ [ppm]	17^{+66}_{-13}	δx_{M21i}	$0.00071^{+0.00072}_{-0.00074}$	$\sigma_{w,M31z}$ [ppm]	18^{+47}_{-14}
am_{M12g}	$0.00726^{+0.00035}_{-0.00037}$	δy_{M21i}	0.00048 ± 0.00039	am_{M31z}	$-0.000433^{+0.000096}_{-0.000094}$
δx_{M12g}	0.00055 ± 0.00045	$FWHM_{M21i}$	$0.00005^{+0.0008}_{-0.00079}$	δx_{M31z}	$0.00064^{+0.0002}_{-0.00019}$
δy_{M12g}	$0.00018^{+0.00053}_{-0.00051}$	c_{M21z}	$-0.00032^{+0.00029}_{-0.00028}$	δy_{M31z}	-0.00018 ± 0.00016
$FWHM_{M12g}$	-0.0003 ± 0.00039	$\sigma_{w,M21z}$ [ppm]	4490 ± 140	$FWHM_{M31z}$	0.00021 ± 0.00025
$peak_{M12g}$	$-0.00163^{+0.00041}_{-0.00039}$	am_{M21z}	0.00073 ± 0.00039	$peak_{M31z}$	-0.00035 ± 0.00023
c_{M12r}	$-0.00065^{+0.00022}_{-0.00021}$	δx_{M21z}	$0.00062^{+0.00058}_{-0.00059}$	c_{OMM}	$0.00183^{+0.00032}_{-0.00033}$
$\sigma_{w,M12r}$ [ppm]	130^{+150}_{-81}	δy_{M21z}	$0.00019^{+0.00031}_{-0.00029}$	$\sigma_{w,OMM}$ [ppm]	1331^{+97}_{-95}
am_{M12r}	0.00095 ± 0.00012	$FWHM_{M21z}$	$-0.00044^{+0.00069}_{-0.00065}$	am_{OMM}	0.00019 ± 0.00013
δx_{M12r}	-0.00029 ± 0.00024	c_{M22i}	$0.00001^{+0.00022}_{-0.00023}$	bg_{OMM}	$0.0022^{+0.00032}_{-0.00033}$
δy_{M12r}	-0.00037 ± 0.00019	$\sigma_{w,M22i}$ [ppm]	2165^{+86}_{-79}	c_{LCO1}	0.00036 ± 0.00021
$FWHM_{M12r}$	-0.00071 ± 0.00023	am_{M22i}	0.00035 ± 0.00027	$\sigma_{w,LCO1}$ [ppm]	903^{+95}_{-90}
$peak_{M12r}$	-0.00055 ± 0.00022	δx_{M22i}	-0.00011 ± 0.00032	am_{LCO1}	-0.00083 ± 0.00015
c_{M12z}	0.00028 ± 0.00021	δy_{M22i}	$-0.00005^{+0.00039}_{-0.00038}$	c_{LCO2}	-0.0 ± 0.00019
$\sigma_{w,M12z}$ [ppm]	21^{+77}_{-17}	$FWHM_{M22i}$	$-0.00007^{+0.00032}_{-0.00033}$	$\sigma_{w,LCO2}$ [ppm]	740^{+65}_{-60}
am_{M12z}	$-0.00063^{+0.00012}_{-0.00011}$	c_{M22z}	0.00005 ± 0.00021	bg_{LCO2}	0.00028 ± 0.0002
δx_{M12z}	-0.00007 ± 0.00018	$\sigma_{w,M22z}$ [ppm]	2033^{+70}_{-68}		

Note. The auxiliary parameters used to detrend each light curve are summarized in Table 2, and the associated coefficient in the table represents the best-fitting value when each vector is normalized to have a maximum of 1 and a minimum of −1.

Table A2
Model Priors and Parameters for Pyaneti Fit to the Combined RV Data Set Described in Section 3.3

Parameter	Prior[a]	Final Value[b]
TOI-1685 b Parameters		
Orbital period P_{orb} (days)	$\mathcal{N}[0.66913923, 0.00000040]$	$0.66913924 \pm 0.00000042$
Transit epoch T_0 ($BJD_{TDB} - 2450000$)	$\mathcal{N}[9910.93830, [0.00038]$	$9910.93828^{+0.00041}_{-0.00039}$
Orbital eccentricity e	$\mathcal{F}[0]$	0
Doppler semiamplitude variation K (m s^{-1})	$\mathcal{U}[0, 50]$	$3.76^{+0.39}_{-0.38}$
GP Hyperparameters		
GP period P_{GP} (days)	$\mathcal{U}[17, 20]$	$18.15^{+0.39}_{-0.36}$
λ_p	$\mathcal{U}[0.01, 2]$	$0.43^{+0.24}_{-0.16}$
λ_e (days)	$\mathcal{U}[1, 150]$	$50.8^{+41.5}_{-21.0}$
A_0	$\mathcal{U}[0, 1.5]$	$0.0066^{+0.0032}_{-0.0015}$
A_1	$\mathcal{F}[0]$	0
Other Parameters[c]		
σ_{RV} CARMENES (m s^{-1})	$\mathcal{J}[1, 100]$	$3.01^{+0.71}_{-0.89}$
σ_{RV} IRD (m s^{-1})	$\mathcal{J}[1, 100]$	$0.79^{+1.02}_{-0.58}$
σ_{RV} MAROON-X Blue 2020 (m s^{-1})	$\mathcal{J}[1, 100]$	$1.03^{+0.76}_{-0.74}$
σ_{RV} MAROON-X Red 2020 (m s^{-1})	$\mathcal{J}[1, 100]$	$1.37^{+0.53}_{-0.43}$
σ_{RV} MAROON-X Blue 2021 (m s^{-1})	$\mathcal{J}[1, 100]$	$0.86^{+0.96}_{-0.62}$
σ_{RV} MAROON-X Red 2020 (m s^{-1})	$\mathcal{J}[1, 100]$	$1.09^{+0.79}_{-0.59}$
γ_{RV} CARMENES (m s^{-1})	$\mathcal{U}[-5, 5]$	$-1.4^{+3.0}_{-3.8}$
γ_{RV} IRD (m s^{-1})	$\mathcal{U}[-5, 5]$	$-2.1^{+3.4}_{-3.6}$

Table A2
(Continued)

Parameter	Prior[a]	Final Value[b]
γ_{RV} MAROON-X Blue 2020 (m s^{-1})	$\mathcal{U}[-5, 5]$	$-2.1^{+3.7}_{4.2}$
γ_{RV} MAROON-X Red 2020 (m s^{-1})	$\mathcal{U}[-5, 5]$	$-2.1^{+3.6}_{-4.2}$
γ_{RV} MAROON-X Blue 2021 (m s^{-1})	$\mathcal{U}[-5, 5]$	$1.1^{+4.3}_{-4.1}$
γ_{RV} MAROON-X Red 2020 (m s^{-1})	$\mathcal{U}[-5, 5]$	$1.1^{+4.3}_{-4.1}$

Notes.
[a] $\mathcal{F}[a]$ refers to a fixed value a, $\mathcal{U}[a, b]$ to a uniform prior between a and b, $\mathcal{N}[a, b]$ to a Gaussian prior with mean a and standard deviation b, and $\mathcal{J}[a, b]$ to the modified Jeffrey's prior as defined by Gregory (2005, Equation (16)).
[b] Inferred parameters and errors are defined as the median and 68.3% credible interval of the posterior distribution.
[c] σ_{RV} is the instrument- and semester-specific RV jitter value, while γ_{RV} is the RV offset applied between the individual data sets.

ORCID iDs

Jennifer A. Burt https://orcid.org/0000-0002-0040-6815
Matthew J. Hooton https://orcid.org/0000-0003-0030-332X
Eric E. Mamajek https://orcid.org/0000-0003-2008-1488
Oscar Barragán https://orcid.org/0000-0003-0563-0493
Sarah C. Millholland https://orcid.org/0000-0003-3130-2282
Tyler R. Fairnington https://orcid.org/0000-0002-0692-7822
Chloe Fisher https://orcid.org/0000-0003-0652-2902
Samuel P. Halverson https://orcid.org/0000-0003-1312-9391
Chelsea X. Huang https://orcid.org/0000-0003-0918-7484
Madison Brady https://orcid.org/0000-0003-2404-2427
Andreas Seifahrt https://orcid.org/0000-0003-4526-3747
Eric Gaidos https://orcid.org/0000-0002-5258-6846
Rafael Luque https://orcid.org/0000-0002-4671-2957
David Kasper https://orcid.org/0000-0003-0534-6388
Jacob L. Bean https://orcid.org/0000-0003-4733-6532

References

Allard, F., Homeier, D., Freytag, B., Schaffenberger, W., & Rajpurohit, A. S. 2013, MSAIS, 24, 128
Anders, F., Khalatyan, A., Chiappini, C., et al. 2019, A&A, 628, A94
Astropy Collaboration, Robitaille, T. P., Tollerud, E. J., et al. 2013, A&A, 558, A33
Astropy Collaboration, Price-Whelan, A. M., Sipőcz, B. M., et al. 2018, AJ, 156, 123
Astropy Collaboration, Price-Whelan, A. M., Lim, P. L., et al. 2022, ApJ, 935, 167
Bai, Y., Liu, J., Wicker, J., et al. 2018, ApJS, 235, 16
Bailer-Jones, C. A. L., Rybizki, J., Fouesneau, M., Demleitner, M., & Andrae, R. 2021, AJ, 161, 147
Barragán, O., Aigrain, S., Rajpaul, V. M., & Zicher, N. 2022, MNRAS, 509, 866
Barragán, O., Aigrain, S., Kubyshkina, D., et al. 2019, MNRAS, 490, 698
Batalha, N. E., Kempton, E. M. R., & Mbarek, R. 2017, ApJL, 836, L5
Batalha, N. E., Lewis, T., Fortney, J. J., et al. 2019, ApJL, 885, L25
Bayo, A., Rodrigo, C., Barrado Y Navascués, D., et al. 2008, A&A, 492, 277
Bell, C. P. M., Mamajek, E. E., & Naylor, T. 2015, MNRAS, 454, 593
Benitez, N., Dupke, R., Moles, M., et al. 2014, arXiv:1403.5237
Benneke, B., Mikal-Evans, T., Acuna, L., et al. 2023, Exploring the existence and diversity of volatile-rich water worlds, JWST Proposal. Cycle 2, ID. #4098
Bevington, P. R., & Robinson, D. K. 1992, Data Reduction and Error Analysis for the Physical Sciences (New York: McGraw-Hill Education)
Birky, J., Hogg, D. W., Mann, A. W., & Burgasser, A. 2020, ApJ, 892, 31
Bluhm, P., Pallé, E., Molaverdikhani, K., et al. 2021, A&A, 650, A78
Bohlin, R. C., Deustua, S. E., & de Rosa, G. 2019, AJ, 158, 211
Boisse, I., Bouchy, F., Hébrard, G., et al. 2011, A&A, 528, A4
Bonfils, X., Delfosse, X., Udry, S., et al. 2005, A&A, 442, 635
Burnham, K., & Anderson, D. 2002, Model selection and multimodel inference: a practical information-theoretic approach (Berlin: Springer Verlag)
Burt, J., Holden, B., Wolfgang, A., & Bouma, L. G. 2018, AJ, 156, 255
Burt, J., Feng, F., Holden, B., et al. 2021, AJ, 161, 10
Caffau, E., Ludwig, H. G., Steffen, M., Freytag, B., & Bonifacio, P. 2011, SoPh, 268, 255
Cenarro, A. J., Moles, M., Cristóbal-Hornillos, D., et al. 2019, A&A, 622, A176
Chakrabarti, A., & Ghosh, J. K. 2011, in Philosophy of Statistics, Handbook of the Philosophy of Science, ed. P. S. Bandyopadhyay & M. R. Forster, Vol. 7 (Amsterdam: North-Holland), 583
Coughlin, J. L., Thompson, S. E., Bryson, S. T., et al. 2014, AJ, 147, 119
Curtis, J. L., Agüeros, M. A., Matt, S. P., et al. 2020, ApJ, 904, 140
Cutri, R. M., Skrutskie, M. F., van Dyk, S., et al. 2003, yCat, II/246
Cutri, R. M., Wright, E. L., Conrow, T., et al. 2012, Explanatory Supplement to the WISE All-Sky Data Release Products, Tech. rep.
Dai, F., Winn, J. N., Gandolfi, D., et al. 2017, AJ, 154, 226
Di Maio, C., Changeat, Q., Benatti, S., & Micela, G. 2023, A&A, 669, A150
Ding, M.-Y., Shi, J.-R., Wu, Y., et al. 2022, ApJS, 260, 45
Doyon, R., Hutchings, J. B., Beaulieu, M., et al. 2012, Proc. SPIE, 8442, 84422R
Dungee, R., van Saders, J., Gaidos, E., et al. 2022, ApJ, 938, 118
ESA 1997, in ESA Special Publication, The HIPPARCOS and TYCHO catalogues. Astrometric and photometric star catalogues derived from the ESA HIPPARCOS Space Astrometry Mission (Paris: European Space Agency)
Espinoza, N., Kossakowski, D., & Brahm, R. 2019, MNRAS, 490, 2262
Essack, Z., Seager, S., & Pajusalu, M. 2020, ApJ, 898, 160
Fisher, C., Akin, C. J., Allen, N., et al. 2023, Constraining the Oxidation State of the Super-Earth TOI-1685 b, JWST Proposal. Cycle 2, ID. #4195
Foreman-Mackey, D., Agol, E., Angus, R., & Ambikasaran, S. 2017, AJ, 154, 220
Gagné, J., Mamajek, E. E., Malo, L., et al. 2018, ApJ, 856, 23
Gaia Collaboration, Brown, A. G. A., Vallenari, A., et al. 2021, A&A, 649, A1
Gaidos, E., Claytor, Z., Dungee, R., Ali, A., & Feiden, G. A. 2023, MNRAS, 520, 5283
Gibson, N. P. 2014, MNRAS, 445, 3401
Gott, J., Richard, I., Vogeley, M. S., Podariu, S., & Ratra, B. 2001, ApJ, 549, 1
Gregory, P. C. 2005, ApJ, 631, 1198
Guerrero, N. M., Seager, S., Huang, C. X., et al. 2021, ApJS, 254, 39
Hardegree-Ullman, K. K., Apai, D., Bergsten, G. J., Pascucci, I., & López-Morales, M. 2023, AJ, 165, 267
Hatzes, A. P. 2013, AN, 334, 616
Hatzes, A. P., Fridlund, M., Nachmani, G., et al. 2011, ApJ, 743, 75
Henden, A. A., Templeton, M., Terrell, D., et al. 2016, yCat, II/336
Higson, E., Handley, W., Hobson, M., & Lasenby, A. 2019, Stat. Comput., 29, 891
Hirano, T., Kuzuhara, M., Kotani, T., et al. 2020, PASJ, 72, 93
Hirano, T., Livingston, J. H., Fukui, A., et al. 2021, AJ, 162, 161
Jackson, B., Jensen, E., Peacock, S., Arras, P., & Penev, K. 2016, CeMDA, 126, 227
Jackson, B., Stark, C. C., Adams, E. R., Chambers, J., & Deming, D. 2013, ApJ, 779, 165
Jakobsen, P., Ferruit, P., Alves de Oliveira, C., et al. 2022, A&A, 661, A80

Jenkins, J. M., Twicken, J. D., McCauliff, S., et al. 2016, Proc. SPIE, 9913, 99133E
Johnson, J. A., & Apps, K. 2009, ApJ, 699, 933
Jönsson, H., Holtzman, J. A., Allende Prieto, C., et al. 2020, AJ, 160, 120
Kempton, E. M.-R., Bean, J. L., Louie, D. R., et al. 2018, PASP, 130, 114401
Kervella, P., Arenou, F., & Thévenin, F. 2022, A&A, 657, A7
Kipping, D. M. 2013, MNRAS, 435, 2152
Kirkpatrick, J. D., Henry, T. J., McCarthy, & Donald, W. J. 1991, ApJS, 77, 417
Kotani, T., Tamura, M., Nishikawa, J., et al. 2018, Proc. SPIE, 10702, 1070211
Kreidberg, L. 2015, PASP, 127, 1161
Laliotis, K., Burt, J. A., Mamajek, E. E., et al. 2023, AJ, 165, 176
Lallement, R., Capitanio, L., Ruiz-Dern, L., et al. 2018, A&A, 616, A132
Lindegren, L., Klioner, S. A., Hernández, J., et al. 2021, A&A, 649, A2
Lopez, E. D. 2017, MNRAS, 472, 245
Lu, H.-P., Zhang, L.-Y., Shi, J., et al. 2019, ApJS, 243, 28
Luque, R., & Pallé, E. 2022, Sci, 377, 1211
Luque, R., Bean, J. L., Changeat, Q., et al. 2023, The First Atmospheric Study of a Bona Fide Water World, JWST Proposal. Cycle 2, ID. #3263
Lutgens, F. K., Tarbuck, E. J., & Tasa, D. G. 2014, in Essentials of geology, ed. P. Higher (London: Pearson Higher Ed)
Lutz, T. E., & Upgren, A. R. 1980, AJ, 85, 1390
Mainzer, A., Bauer, J., Grav, T., et al. 2011, ApJ, 731, 53
Mamajek, E. E., Torres, G., Prsa, A., et al. 2015, arXiv:1510.06262
Mandel, K., & Agol, E. 2002, ApJL, 580, L171
Mann, A. W., Feiden, G. A., Gaidos, E., Boyajian, T., & von Braun, K. 2015, ApJ, 804, 64
Mann, A. W., & von Braun, K. 2015, PASP, 127, 102
Mann, A. W., Dupuy, T., Kraus, A. L., et al. 2019, ApJ, 871, 63
Marfil, E., Tabernero, H. M., Montes, D., et al. 2021, A&A, 656, A162
Millholland, S. C., & Spalding, C. 2020, ApJ, 905, 71
Montegriffo, P., De Angeli, F., Andrae, R., et al. 2023, A&A, 674, A3
Montet, B. T. 2018, RNAAS, 2, 28
Morrell, S., & Naylor, T. 2019, MNRAS, 489, 2615
Morris, R. L., Twicken, J. D., Smith, J. C., et al. 2017, Kepler Science Document KSCI-19081-002, Edited by Jon M. Jenkins, Tech. rep. 6
Mortier, A., & Collier Cameron, A. 2017, A&A, 601, A110
Muirhead, P. S., Dressing, C. D., Mann, A. W., et al. 2018, AJ, 155, 180
Müller, S., Baron, J., Helled, R., Bouchy, F., & Parc, L. 2024, A&A, 686, A296
Narita, N., Fukui, A., Kusakabe, N., et al. 2015, JATIS, 1, 045001
Narita, N., Fukui, A., Yamamuro, T., et al. 2019, JATIS, 5, 015001
Narita, N., Fukui, A., Yamamuro, T., et al. 2020, Proc. SPIE, 11447, 114475K
NASA TOPS Open Science 101 Curriculum Development Team, Adams, A., Almarzouq, B., et al. 2023, NASA TOPS Open Science 101, v1.0, Zenodo, doi:10.5281/ZENODO.10161527
Nava, C., López-Morales, M., Haywood, R. D., & Giles, H. A. C. 2020, AJ, 159, 23
Neves, V., Bonfils, X., Santos, N. C., et al. 2013, A&A, 551, A36
Newton, E. R., Charbonneau, D., Irwin, J., & Mann, A. W. 2015, ApJ, 800, 85
Olney, R., Kounkel, M., Schillinger, C., et al. 2020, AJ, 159, 182
Pancino, E., Sanna, N., Altavilla, G., et al. 2021, MNRAS, 503, 3660
Pancino, E., Marrese, P. M., Marinoni, S., et al. 2022, A&A, 664, A109
Patel, J. A., & Espinoza, N. 2022, AJ, 163, 228
Pecaut, M. J., & Mamajek, E. E. 2013, ApJS, 208, 9
Petrovich, C., Deibert, E., & Wu, Y. 2019, AJ, 157, 180
Pu, B., & Lai, D. 2019, MNRAS, 488, 3568
Queiroz, A. B. A., Anders, F., Chiappini, C., et al. 2020, A&A, 638, A76
Quirrenbach, A., Amado, P. J., Caballero, J. A., et al. 2014, Proc. SPIE, 9147, 91471F
Reis, W., Corradi, W., de Avillez, M. A., & Santos, F. P. 2011, ApJ, 734, 8
Ricker, G. R., Winn, J. N., Vanderspek, R., et al. 2015, JATIS, 1, 014003
Rieke, G. H., Su, K., Sloan, G. C., & Schlawin, E. 2022, AJ, 163, 45
Rogers, L. A. 2015, ApJ, 801, 41
Rosenthal, L. J., Fulton, B. J., Hirsch, L. A., et al. 2021, ApJS, 255, 8
Sanchis-Ojeda, R., Rappaport, S., Winn, J. N., et al. 2014, ApJ, 787, 47
Sarmento, P., Rojas-Ayala, B., Delgado Mena, E., & Blanco-Cuaresma, S. 2021, A&A, 649, A147
Schlaufman, K. C., & Laughlin, G. 2010, A&A, 519, A105
Schweitzer, A., Passegger, V. M., Cifuentes, C., et al. 2019, A&A, 625, A68
Sebastian, D., Gillon, M., Ducrot, E., et al. 2021, A&A, 645, A100
Seifahrt, A., Bean, J. L., Stürmer, J., et al. 2016, Proc. SPIE, 9908, 990818
Seifahrt, A., Stürmer, J., Bean, J. L., & Schwab, C. 2018, Proc. SPIE, 10702, 107026D
Seifahrt, A., Bean, J. L., Stürmer, J., et al. 2020, Proc. SPIE, 11447, 114471F
Seifahrt, A., Bean, J. L., Kasper, D., et al. 2022, Proc. SPIE, 12184, 121841G
Shabram, M., Demory, B.-O., Cisewski, J., Ford, E. B., & Rogers, L. 2016, ApJ, 820, 93
Skilling, J. 2004, in AIP Conf. Ser. 735, Bayesian Inference and Maximum Entropy Methods in Science and Engineering: 24th Int. Workshop on Bayesian Inference and Maximum Entropy Methods in Science and Engineering, ed. R. Fischer, R. Preuss, & U. V. Toussaint (Melville, NY: AIP), 395
Skilling, J. 2006, BayAn, 1, 833
Smith, J. C., Stumpe, M. C., Van Cleve, J. E., et al. 2012, PASP, 124, 1000
Soubiran, C., Brouillet, N., & Casamiquela, L. 2022, A&A, 663, A4
Speagle, J. S. 2020, MNRAS, 493, 3132
Sprague, D., Culhane, C., Kounkel, M., et al. 2022, AJ, 163, 152
Stassun, K. G., Oelkers, R. J., Paegert, M., et al. 2019, AJ, 158, 138
Stumpe, M. C., Smith, J. C., Catanzarite, J. H., et al. 2014, PASP, 126, 100
Stumpe, M. C., Smith, J. C., Van Cleve, J. E., et al. 2012, PASP, 124, 985
Suárez Mascareño, A., González Hernández, J. I., Rebolo, R., et al. 2017, A&A, 597, A108
Terrien, R. C., Mahadevan, S., Deshpande, R., & Bender, C. F. 2015, ApJS, 220, 16
Twicken, J. D., Clarke, B. D., Bryson, S. T., et al. 2010, Proc. SPIE, 7740, 774023
Valsecchi, F., Rasio, F. A., & Steffen, J. H. 2014, ApJL, 793, L3
Van Eylen, V., Albrecht, S., Huang, X., et al. 2019, AJ, 157, 61
Vines, J. I., & Jenkins, J. S. 2022, MNRAS, 513, 2719
Wenger, M., Ochsenbein, F., Egret, D., et al. 2000, A&AS, 143, 9
Winn, J. N., Sanchis-Ojeda, R., Rogers, L., et al. 2017, AJ, 154, 60
Xiang, M., Ting, Y.-S., Rix, H.-W., et al. 2019, ApJS, 245, 34
Yu, J., Khanna, S., Themessl, N., et al. 2023, ApJS, 264, 41
Zechmeister, M., Reiners, A., Amado, P. J., et al. 2018, A&A, 609, A12
Zeng, L., Sasselov, D. D., & Jacobsen, S. B. 2016, ApJ, 819, 127
Zhang, B., Liu, C., & Deng, L.-C. 2020, ApJS, 246, 9
Zhang, M., Hu, R., Inglis, J., et al. 2024, ApJL, 961, L44
Zhong, J., Lépine, S., Hou, J., et al. 2015, AJ, 150, 42